Capillary pressure heterogeneity and hysteresis for the supercritical CO_2/water system in a sandstone

Ronny Pini[a,*], Sally M Benson[b]

[a]*Department of Chemical Engineering, Imperial College London, London, UK*
[b]*Department of Energy Resources Engineering, Stanford University, Stanford (CA), USA*

Abstract

We report results from an experimental investigation on the hysteretic behaviour of the capillary pressure curve for the supercritical CO_2-water system in a Berea Sandstone core. Previous observations have highlighted the importance of sub-core-scale capillary heterogeneity in developing local saturations during drainage; we show in this study that the same is true for the imbibition process. Spatially distributed drainage and imbibition scanning curves were obtained for mm-scale subsets of the rock sample non-invasively using X-ray CT imagery. Core- and sub-core scale measurements are well described using the Brooks-Corey formalism, which uses a linear trapping model to compute mobile saturations during imbibition. Capillary scaling yields two separate universal drainage and imbibition curves that are representative of the full sub-core scale data set. This enables accurate parameterisation of rock properties at the sub-core scale in terms of capillary scaling factors and permeability, which in turn serve as effective indicators of heterogeneity at the same scale even when hysteresis is a factor. As such, the proposed core-analysis workflow is quite general and provides the required information to populate numerical models that can be used to extend core-flooding experiments to conditions prevalent in the subsurface, which would be otherwise not attainable in the laboratory.

Keywords: core analysis, multi-phase flow, capillary heterogeneity

---

*Corresponding author
Email address:* r.pini@imperial.ac.uk (Ronny Pini)

---

1. Introduction

Hysteresis is a basic aspect of multiphase flow in porous media that affects systems in the subsurface, where situations of repeated drainage and imbibition events are often encountered. Cyclic boundary conditions are seen in the natural

5 fluctuation of the water table in soils (Lehmann et al., 1998) or are induced artificially, such as during so-called Water-Alternating-Gas (WAG) injection schemes for Enhanced Oil Recovery (EOR) processes (Blunt et al., 1993; Kovscek and Cakici, 2005). In this study we consider the geological storage of CO_2 in deep saline aquifers, where hysteresis is primarily associated with imbibition at the

10 trailing edge of a migrating CO_2 plume. This phenomenon is key toward the effective immobilisation of CO_2 by capillary trapping, a process resulting from the break-up of the CO_2 phase into isolated ganglia (Juanes et al., 2006). A recent review of published experimental data reports that $10 - 40\%$ of the available rock's pore volume can ultimately be retained in the storage formation by

15 capillary trapping (Krevor et al., 2015), thus confirming early indications from the seminal work by the Intergovernmental Panel on Climate Change (IPCC) on the importance of this mechanism throughout the life of a CO_2 injection and storage operation (IPCC, 2005). In analogy to EOR processes, the potential exist to further maximise trapping in the storage formation by devising appro-

20 priate brine/CO_2 injection schemes, such as Water-Alternating-Gas (WAG) (Ide et al., 2007; Qi et al., 2009; Cameron and Durlofsky, 2012). Because they are key input parameters used in reservoir simulators, so-called multiphase characteristic curves (relative permeability *and* capillary pressure curves) need to properly account for hysteresis in order to provide reliable estimates of plume spreading

25 and trapping (Doughty, 2007). This becomes a necessity when potential stores are evaluated where structural trapping is uncertain or even absent.

The (re)distribution of fluids in reservoir rocks is largely controlled by buoyancy and capillary action. The relationship between capillary pressure and

2

saturation is conventionally described through a characteristic curve relating, P_c, to the wetting phase (WP) saturation, S_w. This basic constitutive relation can be regarded as the fingerprint of a rock, because it carries information on the structure of the pore space (e.g., pore-size distribution and tortuosity), and on its interaction with reservoir fluids (e.g., surface tension) (Anderson, 1987). When representative fluids are directly used in the experiments, capillary pressure data can also be used to infer information on the wetting state of the porous rock (Pini et al., 2012; Al-Menhali et al., 2015). Key to the analysis of immiscible displacements in porous media is that saturation hysteresis leads to different $P_c - S_w$ curves for describing drainage and imbibition processes (Haines, 1930). As such, there is virtually an infinite number of intermediate (scanning) curves that can be obtained depending on the point at which the direction of saturation change is reversed from drainage to imbibition, and vice-versa (Morrow and Harris, 1965). With reference to the CO_2/brine system, only a limited number of studies reports capillary pressure hysteresis data at conditions associated with CO_2 injection at depth, i.e. where CO_2 is in supercritical (sc) phase. Bounding drainage and imbibition $P_c - S_w$ curves are available for unconsolidated homogeneous media, including quartz (Plug and Bruining, 2007; Tokunaga et al., 2013) and limestone/dolomite sands (Wang and Tokunaga, 2015), while observations on consolidated systems are still limited to primary drainage conditions and to a small number of rock types (Pentland et al., 2011; Pini et al., 2012; El-Maghraby and Blunt, 2012). As a matter of fact, hysteresis data in the form of $P_c - S_w$ scanning curves are practically inexistent for rocks and the few available are limited to equivalent wetting conditions (air/brine at room temperature) (Raeesi et al., 2014). Notably, several studies have addressed hysteresis by investigating end-points characteristics of scCO$_2$-brine-rock systems; these report values of residual nonwetting phase (NWP) saturation as a function of the initial (or turning point) NWP saturation (the maximum value attained during drainage), and parameterise them in terms of so-called initial-residual (IR) curves (Pentland et al., 2011; El-Maghraby and Blunt, 2012; Krevor et al., 2012; Akbarabadi and Piri, 2013; Li et al., 2015; Niu et al., 2015). In the absence of direct ex-

3

perimental data, an IR curve can be used to calculate imbibition bounding and scanning curves from non-hysteretic (i.e. drainage) formulations of characteristic flow functions. While this approach has been widely employed to produce hysteretic relative permeability curves (Land, 1968; Qi et al., 2009), validation by means of experiments with the $scCO_2$/water system has only recently begun (Ruprecht et al., 2014). To our knowledge and despite its general applicability, this simple approach hasn't been applied to parameterise models for hysteresis in the capillary pressure, other than for qualitative illustration purposes (Krevor et al., 2015).

Although they are inherently limited in the accessible length-scale, laboratory measurements on reservoir core samples still represent the only way to make direct observations on multiphase flow-properties. Yet, properties derived on these samples are of limited use and should be regarded as sample-specific or "pseudos" (Ringrose et al., 1993), if the presence of sub-core scale heterogeneities is not accounted for in data processing and interpretation (Ganapathy et al., 1993; Huang et al., 1995; Egermann and Lenormand, 2005; Krause et al., 2013). The advent of imaging technology has significantly reshaped the landscape of so-called Special Core Analysis (SCAL) by providing unprecedented insight on rock structure and processes down to the scale of a single pore throat (i.e. the scale at which all reservoir processes operate) (Shafer, 2013). Most significantly, such developments have revealed that results must be interpreted by acknowledging the fact that capillary pressure heterogeneity results into local saturation development (Graue, 1994; Chaouche et al., 1994; Shi et al., 2011; Pini et al., 2012; Alemu et al., 2013; Oh et al., 2015; Ott et al., 2015), which may lead to apparent flow rate effects on macroscopic properties of relative permeability and residual trapping (Perrin and Benson, 2010; Krevor et al., 2011; Kuo and Benson, 2015; Reynolds and Krevor, 2015). Accordingly, improved laboratory workflows are now being developed that make use of such wealth of information by e.g., referring to the internal structure of the sample and in-situ observations, to obtain accurate parameterisation of rock and multiphase properties (Pini and Benson, 2013a). However, most studies so-far have focused on

drainage displacements and the degree to which sub-core scale heterogeneities control the imbibition process is still uncertain.

In this study, we report on the development of such workflow and on its application to the study of the hysteretic behaviour of the capillary pressure curve at the core- and sub-core-scale for the $scCO_2$/water/Berea Sandstone system. The remaining of the paper is structured as follows. In Section 2, a hysteretic model is presented for the capillary pressure function that is based on the Brooks-Corey formulation and that is required for the analysis of the experimental data. This is followed by a capillary scaling analysis that yields separate universal drainage and imbibition functions. The core-flooding experimental procedure is described next (Section 3), together with the workflow adopted for in-situ measurement of scanning $P_c(S)$ curves and interpretation (Section 4). We then present the experimental results (Section 5) that include core- and sub-core scale fluid saturation distributions, NWP trapping and capillary pressure curves. Section 6 includes a discussion on the capillary scaling behaviour in the presence of hysteresis, which can be used for the accurate parameterisation of rock properties at the sub-core scale.

2. Theory

2.1. Capillary pressure hysteretic model

Drainage capillary pressure-saturation data for gas/liquid systems are often described using the Brooks-Corey (BC) function (Brooks and Corey, 1964),

$$P_c^D = P_e \widehat{S}_w^{-1/\lambda} \quad \text{for} \quad 0 \leq \widehat{S}_w \leq 1 \tag{1}$$

where P_e is the capillary entry pressure (or '*bubbling pressure*' in Brooks and Corey (1964)), λ is the so-called pore-size distribution index and $\widehat{S}_w$ is the effective wetting phase (WP) saturation. The latter is defined as:

$$\widehat{S}_w = \frac{S_w - S_{w,irr}}{1 - S_{w,irr}} \tag{2}$$

5

where S_{w} is the WP saturation and $S_{\text{w,irr}}$ is the irreducible WP saturation. Because the BC model is a correct qualitative form to represent a capillary pressure curve, a reasonably good fit over a quite wide saturation range of many experimental data can be obtained by appropriate choice of the parameters P_{e}, λ and $S_{\text{w,irr}}$. Systems that have been successfully described include both unconsolidated and consolidated porous media with a wide range of pore-size distributions ($\lambda = 0.5 - 7.5$) (Brooks and Corey, 1964), in addition to the Berea Sandstone rock type considered in this study ($\lambda = 1.4 - 2.7$) (Krevor et al., 2012; Pini and Benson, 2013b; Al-Menhali et al., 2015). In the original contribution by Brooks and Corey (1964), the authors anticipated that Eq. 1 is only valid for $P_{\text{c}}^{\text{D}} \geq P_{\text{e}}$ and "*possibly only for the drainage cycle*"; additionally, because of entrapment of the nonwetting phase (NWP) following a WP saturation increase, the observed relationship among capillary pressure and saturation is usually not the same for drainage and imbibition, giving rise to hysteretic behaviour (Haines, 1930). In analogy to approaches used for developing relative permeability hysteretic models (Land, 1968), we propose here to compute the capillary pressure during imbibition, P_{c}^{I}, based on an effective *mobile* NWP saturation, while using the same functional form of the drainage $P_{\text{c}}(S)$ curve, i.e.

$$P_{\text{c}}^{\text{I}} = P_{\text{c,i}} \left(\widehat{S}_{\text{w,m}}^{-1/\lambda} - 1 \right) \quad \text{for} \quad \widehat{S}_{\text{w,i}} \leq \widehat{S}_{\text{w,m}} \leq 1 \tag{3}$$

where $\widehat{S}_{\text{w,m}}$ is the effective WP saturation balancing the *mobile* NWP saturation ($\widehat{S}_{\text{w,m}} + \widehat{S}_{\text{nw,m}} = 1$) and $\widehat{S}_{\text{w,i}}$ is the corresponding value at the point of flow reversal (turning point). $P_{\text{c,i}}$ is defined from the condition that holds at the turning point, i.e. $P_{\text{c}}^{\text{D}}(\widehat{S}_{\text{w,i}}) = P_{\text{c}}^{\text{I}}(\widehat{S}_{\text{w,i}})$ and that is solved upon combination of Eqs. 1 and 3 and rearranging:

$$P_{\text{c,i}} = P_{\text{e}} \left(1 - \widehat{S}_{\text{w,i}}^{1/\lambda} \right)^{-1} \tag{4}$$

where $\widehat{S}_{\text{w,i}}$ is constant along the given imbibition branch and the remaining parameters are known from the drainage curve. A few remarks are worth making here. First, the use of a mobile saturation in Eq. 3 is necessary, because

6

the latter is associated to the fraction of NWP that is continuous throughout the pore space and that is therefore the sole contributor to the value of the capillary pressure that is measured experimentally. Secondly, while other parametric relationships of similar simplicity have been defined by others (e.g., Li and Horne (2001)), Eq. 3 additionaly maintains the exact same functional form as the drainage curve, i.e. $P_\mathrm{c} \propto \widehat{S}^{-1/\lambda}$, thus ensuring that the underlying microscopic pore-space geometry (as defined through the parameter λ) is preserved in the hysteretic model. Third, in the proposed interpretation of the BC model, we relax the original definition of the entry pressure parameter ("*a measure of the maximum pore-size forming a continuous network of flow channels within the medium*"); data from the literature (e.g., Morrow and Harris (1965); Anderson (1987)) consistently show that the capillary pressure changes very steeply near full wetting conditions, before any significant change in saturation can be observed. The parameter P_e is therefore not a "true" entry pressure and it is not surprising that P_c values are often observed during imbibition that are well below the BC-predicted entry pressure, suggesting that a continuous NWP pathway does exist that may have not been accessible during the initial drainage phase. Fourth, as with any other formulation, the use of Eq. 3 requires the adoption of a trapping model to compute the amount of mobile saturation along the imbibition path. As described in the Introduction, these trapping models are usually parameterised in the form of IR curves, which take the general form, $\widehat{S}_\mathrm{nw,r} = f(\widehat{S}_\mathrm{nw,i})$, where $\widehat{S}_\mathrm{nw,r}$ is the residual saturation, i.e. the saturation at which the imbibition curve terminates and the continuum scale capillary pressure goes to zero. As shown in Appendix A.1, closed-form expressions for the mobile NWP saturation can be derived upon adoption of a linear trapping model, $\widehat{S}_\mathrm{nw,r} = C\widehat{S}_\mathrm{nw,i}$ (Ruprecht et al., 2014),

$$\widehat{S}_\mathrm{nw,m} = \frac{\widehat{S}_\mathrm{nw} - C\widehat{S}_\mathrm{nw,i}}{1 - C} \tag{5}$$

or the Land trapping model, $\widehat{S}_{\mathrm{nw,r}} = \widehat{S}_{\mathrm{nw,i}}/(1 + C_{\mathrm{L}}\widehat{S}_{\mathrm{nw,i}})$ (Land, 1968),

$$\widehat{S}_{\mathrm{nw,m}} = \frac{1}{2}\left[-\Delta + \sqrt{\Delta^2 - 4\Delta/C_{\mathrm{L}}}\right] \tag{6}$$

with $\Delta = \widehat{S}_{\mathrm{nw,r}}(\widehat{S}_{\mathrm{nw,i}}) - \widehat{S}_{\mathrm{nw}}$. Thus, the value of $\widehat{S}_{\mathrm{nw,m}}$ can be readily estimated in terms of known (i.e. measurable) variables and it can be used directly in Eq. 3 to determine the imbibition capillary pressure corresponding to given values of the effective NWP saturation, $\widehat{S}_{\mathrm{nw}}$.

2.2. Scaling of Drainage and Imbibition $P_{\mathrm{c}}(S)$ Curves

Scaling approaches are very useful in the analysis of experimental capillary pressure curves, because they enable (i) the comparison of measurements using different fluid pairs on the same porous medium (Tokunaga et al., 2013), as well as (ii) the description of the spatial variability of the $P_{\mathrm{c}} - S$ relationship within the porous medium itself (Pini and Benson, 2013a), by means of a single universal capillary pressure curve, $\Pi_{\mathrm{c}}(S)$. In the following, an approach is proposed that renders imbibition bounding and scanning $P_{\mathrm{c}}(S)$ curves indistinguishable, too, so as to enable examination of capillary heterogeneity at the sub-core scale using separate universal drainage $\Pi_{\mathrm{c}}^{\mathrm{D}}(S)$ and imbibition $\Pi_{\mathrm{c}}^{\mathrm{I}}(S)$ capillary pressure curves.

As proposed by Miller and Miller (1956), the appropriate scaling group for capillary flow in so-called *similar* media is $\{lP_{\mathrm{c}}/\gamma\}$, where l is a characteristic length, which is often set as the representative grain size of the medium (Tokunaga et al., 2013). Instead, we choose here $l = \gamma/P_{\mathrm{e}}$, thus reducing the scaling group to $\{P_{\mathrm{c}}/P_{\mathrm{e}}\}$. Note that the latter implies that such *similar* media possess identical values of the pore-size distribution index λ (Brooks and Corey, 1964), thus ensuring consistency with a $P_{\mathrm{c}} - S$ relationship of the form given by Eqs. 1 and 3; most significantly, the definition of the characteristic length doesn't require the rather limiting condition found in early studies of such media having common wetting characteristics (e.g., contact angle) and porosity (Miller and Miller, 1956). To capture capillary heterogeneity, a scaling factor α_j is introduced that is defined as the ratio of the characteristic length l_j of a system at a

8

location j, and the corresponding value $\widetilde{l}$ of a reference system. For the system considered in this study, i.e. a rock sample consisting of N_{vox} voxels distributed at locations $j = 1...N_{\mathrm{vox}}$, the scaling factor is thus defined as

$$\alpha_j = \frac{l_j}{\widetilde{l}} = \frac{\widetilde{P}_{\mathrm{e}}}{P_{\mathrm{e},j}} \qquad j = 1...N_{\mathrm{vox}} \qquad (7)$$

where the interfacial tension of the given fluid pair, γ, is assumed to be constant and the core-scale is set as the reference characteristic length with a corresponding capillary entry pressure $\widetilde{P}_{\mathrm{e}}$. Accordingly, l_j refers to the scale of a voxel, which in this study has a volume of $(3 \times 3 \times 3)$ mm^3 (see also Section 3). The universal drainage capillary pressure curve is thus given by:

$$\Pi_{\mathrm{c}}^{\mathrm{D}}(\widehat{S}_{\mathrm{w}}) = \frac{\widetilde{P}_{\mathrm{c}}^{\mathrm{D}}(\widehat{S}_{\mathrm{w}})}{\widetilde{P}_{\mathrm{e}}} = \frac{P_{\mathrm{c},j}^{\mathrm{D}}(\widehat{S}_{\mathrm{w}})}{P_{\mathrm{e},j}} = \frac{\alpha_j P_{\mathrm{c},j}^{\mathrm{D}}(\widehat{S}_{\mathrm{w}})}{\widetilde{P}_{\mathrm{e}}} \qquad j = 1...N_{\mathrm{vox}} \qquad (8)$$

and the universal imbibition capillary pressure curve is expressed as follows:

$$\Pi_{\mathrm{c}}^{\mathrm{I}}(\widehat{S}_{\mathrm{w,m}}) = \frac{\widetilde{P}_{\mathrm{c}}^{\mathrm{I}}(\widehat{S}_{\mathrm{w,m}})}{\widetilde{P}_{\mathrm{e}}} = \frac{P_{\mathrm{c},j}^{\mathrm{I}}(\widehat{S}_{\mathrm{w,m}})}{P_{\mathrm{i},j}} = \frac{\alpha_j \beta_j P_{\mathrm{c},j}^{\mathrm{I}}(\widehat{S}_{\mathrm{w,m}})}{\widetilde{P}_{\mathrm{e}}} \qquad j = 1...N_{\mathrm{vox}} \qquad (9)$$

where $\beta_j = 1 - \widehat{S}_{\mathrm{w,i}}^{1/\lambda}$ and where the reference imbibition capillary pressure curve $\widetilde{P}_{\mathrm{c}}^{\mathrm{I}}$ is given by the core-scale bounding curve ($S_{\mathrm{w,i}} = S_{\mathrm{w,irr}}$). We note that upon adoption of the same scaling group $\{P_{\mathrm{c}}/P_{\mathrm{e}}\}$ for both drainage and imbibition processes, we ensure consistency with the formulation of the capillary pressure hysteretic model that uses λ as the sole criterion for similarity. Furthermore, it is worth pointing out that in the proposed scaling approach any variability in microscopic parameters (e.g., contact angle and the surface tension) is embedded in the corresponding variability of the capillary entry pressure. The reason for this is the limited spatial resolution at which quantitative observations can be made with medical CT instruments (in the order of a few mm for this study). Recent advancements in X-ray technology are now enabling direct imaging of fluid-fluid interfaces and contact angles within porous rocks (Andrew et al., 2014), yet at the expenses of sample size (up to several mm). We anticipate that the ability to apply the approach proposed here at such high

9

resolutions will enable creating a direct link between microscopic parameters and the continuum scale, thus probing fundamental questions on the origins of capillary heterogeneity.

2.3. $P_c(S)$ hysteretic model: an illustrative example

Figure 1 (left plot) shows hysteretic capillary pressure curves obtained from Eqs. 1 (drainage) and 3 (imbibition), and upon adopting the linear (dashed lines) and the Land model (solid lines) to describe NWP trapping during the imbibition process. The latter are plotted in the inset of the figure in the form of two IR curves. It can be seen that while the two models use the same maximum value of $S_{nw,r}$, the Land model systematically predicts larger trapping over the whole saturation range. Note, however, that starting from the maximum value of $S_{nw,r}$ and for a given saturation change in the imbibition direction, the amount that is *incrementally* trapped in the Land model is initially less than the (constant) value predicted by the linear model and it gradually increases until it approaches the limit imposed by the identity line. As shown in the figure and for a given turning point saturation, such behaviour produces $P_c(S)$ curves that follow a distinct imbibition path, which for the Land model becomes very steep at low capillary pressure values. On the right-hand side plot of Figure 1 are shown the corresponding universal (scaled) capillary pressure curves that have been obtained from Eqs. 8 (drainage) and 9 (imbibition). It is worth noting that because two separate universal curves are used, each turning point possesses two different Π_c values, depending on whether the drainage or the imbibition branch is considered. Also, because the adopted scaling group uses a *mobile* NWP saturation, imbibition scanning curves are now collapsing into a single, universal $\Pi_c^I(\widehat{S}_{w,m})$ curve. As a consequence, the distinction no longer exists among imbibition scanning curves that originated from the choice of a different trapping model.

10

3. Materials and Experimental Procedure

3.1. Rock Sample

A fired Berea Sandstone core (length: 10 cm, diameter: 5 cm) was used in this study. The sample has a permeabilty of 945 mD (measured with water) and an average porosity of 22% (measured by X-ray CT) with minimal variations at the sub-core scale (maximum deviation from the mean of about 0.2%abs. and 2%abs. for slice- and voxel-averaged values, respectively). A mercury injection capillary pressure (MICP) curve was measured on a small ($\sim$1 cm^3) sister sample using a Micromeritics Autopore IV by covering the pressure range from vacuum to 228 MPa. The MICP curve was corrected to account for unresolved pore space (about 10%rel.) and entry pressure effects (minimum value set to 42 kPa) by following a procedure described in a previous publication (Pini and Benson, 2013b). For comparison against direct measurement using the CO_2/water (12) fluid pair at experimental (core-flood) P,T conditions, the MICP data (HgA) are converted by using the equation $P_{c,12} = P_{c,HgA}\gamma_{12}/\gamma_{HgA}$ (Purcell, 1949), where γ is the interfacial tension, γ_{HgA} is set to 485 mN/m and γ_{12} is used as a fitting parameter. Note that, in agreement with earlier observations on Berea Sandstone (Pini and Benson, 2013b) and other uniformly wetted rocks (Anderson, 1987; Al-Menhali et al., 2015), the contact angle is dropped from the equation, because both systems show a strong wettability preference towards one of the two fluids and roughness effects prevail.

3.2. Core-flooding Experiment

The detailed experimental procedure together with a description of the experimental set-up is given elsewhere (Ruprecht et al., 2014). Carbon dioxide (CO_2) and tap water (salinity less than 50 mg/L) were used as the operating fluids for the core-flooding experiment, which has been carried our at a temperature of 50°C, a pore fluid pressure of 9 MPa and a confining pressure of 13 MPa. At these conditions, the viscosity (in $\times 10^{-5}$ Pa s) and density (in kg/m^3) of CO_2/water are 2.31/54.8 and 285/992. To warrant immiscible

displacement conditions, fluids were mixed and circulated through the core-flooding system overnight. Three cycles of drainage and imbibition displacements were completed to collect steady-state saturation data at various fractional flows, $f_{\text{nw}} = q_{\text{nw}}/q_{\text{tot}}$, where q_{tot} and q_{nw} are the total and nonwetting phase (NWP = CO_2) volumetric flow rates, respectively. A minimum of 10 pore volumes (PV) was allowed to pass through the core at each fractional flow before taking a full X-ray CT scan of the core; attainment of steady state conditions was further confirmed by the observed stable pressure drop (deviations within 5% of the average value) and gas saturation profile along the sample. During the experiment, q_{tot} was kept at 20 ml/min ($u_{\text{tot}} = q_{\text{tot}}/A = 1.7 \times 10^{-4}$ m/s), while the NWP fractional flow was increased or decreased between steps, depending on whether a drainage or imbibition loop was to be completed. The experiment started with the rock sample fully saturated with water; the first and the second cycles (A and B) were interrupted before reaching $f_{\text{nw}} = 1$ (during drainage) and $f_{\text{nw}} = 0$ (during imbibition). The main reason for this was to maintain a relatively uniform saturation within the core, a condition that can indeed be met only during co-injection. Accordingly, the second and third drainage cycles began from previous NWP trapped saturations and not from re-established initial conditions ($S_{\text{w}} = 1$). After reaching $f_{\text{nw}} = 1$ during the final cycle (C), the total NWP flow rate was increased in steps from 20 up to 50 mL/min. A total of about 1000 PV were passed through the sample to complete the multiple drainage-imbibition cycles over a period of 3 days; we note that this time is still very short as compared to the months required to alter the wetting state of rock surfaces by exposure with supercritical CO_2 (Wang and Tokunaga, 2015), as indicated by previous observations on sandstone samples where NWP trapping characteristics were retained upon repeated cycling (Saeedi et al., 2011).

3.3. X-ray CT images acquisition

A medical CT scanning instrument (General Electric Hi-Speed CT/i) was used for acquiring X-ray images of the rock sample during the core-flooding experiment. Voxel-, slice- and core-averaged fluid-phase saturation values were

calculated upon appropriate combination and normalisation of the given sets of scans (Ruprecht et al., 2014). The same set of imaging parameters has been applied throughout the study, namely voxel dimension: $(0.5 \times 0.5 \times 1)$ mm^3; tube current: 200 mA; energy level of the radiation: 120 keV; display field of view: 25 cm. For quantitative analysis, tomograms were resampled into $(3 \times 3 \times 3)$ mm^3 voxels, thereby reducing the uncertainty associated with the computed porosity and saturation values at the voxel scale to 0.34 and 3.4%abs., respectively. Note that this voxel volume contains approximately 4500 grains and is well above the REV size of Berea Sandstone (Pini and Madonna, 2016) and can thus be associated to continuum-scale properties, such as porosity, permeability, fluid saturation, and capillary pressure. Images reconstruction and data analysis were carried out using in-house MATLAB routines.

4. Core-Analysis Workflow

In the following two sections, the approach is described for measuring capillary pressure curves (core- and sub-core scale) from a multi-rate core-flood (NWP injection) as well as for a situation of co-injection of both NWP and WP (drainage and imbibition). To facilitate the description, the two approaches are also depicted in Figure 2, together with a schematic of the high-pressure core holder.

4.1. Core- and Sub-core-scale Scanning $P_c(S)$ Curves

As originally proposed in Ramakrishnan and Cappiello (1991), a core-scale drainage capillary pressure curve can be estimated from a multi-rate core-flood, where a NWP is injected to displace a WP that initially saturates the sample (NWP fractional flow, $f_{nw} = 1$). The $P_c^D(S)$ curve is built by combining steady-state pressure drop values measured across the sample at each flow rate with the corresponding fluid saturations observed (Lenormand et al., 1993) or computed (Ramakrishnan and Cappiello, 1991) at the inlet face of the core. With reference to Berea Sandstone, this method has been recently applied to various

13

gas-liquid pairs, including CO_2-brine and N_2-brine systems, over a wide range of interfacial tension values (30-70 mM/m) and on both intact and fractured samples (Pini et al., 2012; Pini and Benson, 2013b; Oh et al., 2013; Al-Menhali et al., 2015; Li et al., 2015). Most significantly, this experimental approach can be extended to the measurement of subcore-scale $P_c^D(S)$ curves at any position (voxel) within the sample non-invasively (Pini and Benson, 2013a). Two assumptions are required to enable this extension: (i) at each flow rate the fluids are in capillary equilibrium throughout the sample and (ii) the functional relationship between capillary pressure and saturation that is obtained for the inlet slice is valid for any other slice within the sample. We note that condition (i) is met when the relative strengths of viscous to capillary forces and of buoyancy to capillary forces are both small (Wilkinson, 1996):

$$\frac{\Delta P_{\mathrm{visc}}}{\Delta P_{\mathrm{cap}}} = \frac{u_{\mathrm{tot}}\mu_{\mathrm{nw}}r/k}{\gamma_{12}/r} << 1 \quad \text{and} \quad \frac{\Delta P_{\mathrm{buoy}}}{\Delta P_{\mathrm{cap}}} = \frac{\Delta\rho g r}{\gamma_{12}/r} << 1 \qquad (10)$$

where r is the average grain size ($r \sim 100\ \mu$m), used as the characteristic microscopic length. For the experiment conducted in this study both ratios are of order 1×10^{-3}, confirming that capillary forces dominate; this implies that the system behaves in the same way as in the absence of viscous and buoyancy forces and fluid configuration in the pore space is thus solely controlled by the capillary pressure. When these conditions are met, a capillary pressure profile along the length of the sample can be derived from the known core-scale $P_c^D(S)$ functional relationship and slice-averaged saturations measured by X-ray CT; subcore-scale $P_c^D(S)$ curves are constructed by linking these capillary pressure values to the saturation observed in each subset (voxel) of each slice. Alternatively, a constant and uniform saturation throughout the sample can be achieved upon co-injection of both fluid phases at a given fractional flow ($f_{\mathrm{nw}} < 1$) and constant total flow rate; hence, a single (core-averaged) capillary pressure value can be used to obtain $P_c^D(S)$ drainage curves for each voxel in the system. In this study, both approaches (single-phase- and co-injection) have been applied and results combined into a unique data set, so as to cover a wide range of capil-

14

lary pressure values. Furthermore, we extend here the co-injection approach to the measurement of *imbibition* subcore-scale capillary pressure curves. In particular, at a given fractional flow, the mobile core-averaged NWP saturation is estimated from a trapping model (Eqs. 5 or 6, which can be calibrated on direct experimental observations) and the corresponding capillary pressure value is computed from the known imbibition $P_c^I(S)$ functional relationship (Eq. 3, with parameter values known from the experimentally measured drainage curve); again, imbibition subcore-scale capillary pressure curves are then constructed by linking observed voxel saturations to this (average) capillary pressure value.

4.2. Data Processing Workflow

The analysis and interpretation of the whole core-flooding data-set follows the procedure summarised by the workflow depicted in Figure 3. The starting point is the analysis of the multi-rate drainage test, which is used to estimate the core-average (reference) capillary pressure curve for the CO_2/water fluid pair at experimental conditions (Section 4.1). The measured data are calibrated against an independent MICP curve (Section 3.1) and the combined set is subsequently fitted using the Brooks-Corey $P_c^D(S)$ model (Eq. 1). A steady-state 1D displacement model (described in Appendix A.2) is solved to reproduce the slice-averaged saturation profiles observed during the multi-rate core-flood using the obtained $P_c^D(S)$ curve as input. This step is key towards validating (i) the reliability of the measured capillary pressure curve, by confirming that capillary-equilibrium conditions were achieved during the experiment, and (ii) its use for capturing both slice- and core-scale fluid distribution.

The co-injection drainage and imbibition displacements are analysed next. Core-averaged NWP saturations are computed at each fractional flow (f_{nw}^D or f_{nw}^I) for the central portion of the core that is unaffected by end-effects ($L = 2 - 6$ cm $\widehat{=}$ 13 slices $\widehat{=}$ 2379 voxels $= N_{vox}$). For the drainage steps, these are used to compute the corresponding capillary pressure directly from the reference $P_c^D(S)$ drainage curve (Eq. 1). For the imbibition steps, the core-averaged NWP saturations are first used to build an IR curve that is fitted using an

15

appropriate trapping model (Section 2.1); the latter is used to compute core-averaged *mobile* NWP saturations along each imbibition scanning curve and these mobile saturation values are then used alongside the imbibition $P_\mathrm{c}^\mathrm{I}(S_\mathrm{m})$ model (Eq. 3) to estimate the corresponding core-averaged capillary pressure values.

The workflow continues with the analysis of sub-core scale data, which are used to extract voxel-by-voxel drainage and imbibition capillary pressure curves by linking the core-averaged drainage and imbibition P_c values computed above to the observed voxel WP saturations. Sub-core scale *drainage* curves are constructed based on observations from both the co-injection and multi-rate drainage tests, and are used to estimate capillary scaling factors, α_j, by minimising the following objective function,

$$\Phi = \sum_{j=1}^{N_\mathrm{vox}} \sum_{k=1}^{N_\mathrm{pc}} \left[\frac{\alpha_j P_{\mathrm{c},j}^\mathrm{D}(S_{j,k}) - \widetilde{P}_\mathrm{c}^\mathrm{D}(S_{j,k})}{\widetilde{P}_\mathrm{c}^\mathrm{D}(S_{j,k})} \right]^2 \tag{11}$$

For the co-injection experiments, the number of capillary pressure values, N_pc, corresponds to the number of fractional flows ($f_\mathrm{nw}^\mathrm{D} = 7$, see Table 1), while for the multi-rate test, $N_\mathrm{pc} = N_\mathrm{q} \times N_\mathrm{sl}$, with N_q and N_sl being the number of flow rates and slices, respectively. A Matlab built-in function (`fminsearch`) was used to solve the minimisation problem, which was set to terminate when both of the following conditions were satisfied, namely $|f(x_i) - f(x_{i+1})| < \varepsilon(1+|f(x_i)|)$ and $|x_i - x_{i+1}| < \varepsilon(1+|x_i|)$, with $\varepsilon = 1 \times 10^{-12}$. These scaling factors are used to evaluate the universal drainage capillary pressure curve ($\Pi_\mathrm{c}^\mathrm{D}(S)$, Eq. 8) and to build a sub-core scale permeability map of the core sample (see Section 6). Similarly, the voxel-by-voxel imbibition capillary pressure curves are evaluated against the corresponding universal imbibition $\Pi_\mathrm{c}^\mathrm{I}(S_\mathrm{m})$ curve (Eq. 9); to this aim, the required mobile NWP saturation values for each voxel are again computed from Eqs. 5 or 6 by using the observed turning-point *voxel* saturations together with the *core*-scale trapping coefficient (C or C_L). As such, the imbibition model is applied in a fully predictive way, because the required values of the β_j parameters are fully defined from the measured turning-point voxel saturations

16

and the capillary pressure model, while the α_j parameters are already known from the analysis of the drainage data.

5. Results

5.1. Steady-state core-scale saturation profiles

Figure 4 shows the steady-state 1D slice-averaged CO_2 saturation profiles along the length of the core acquired at each fractional flow from X-ray CT measurements. For the sake of better visualisation, all drainage steps are shown in the top-left diagram, while data measured during imbibition are shown in the remaining quadrants for each cycle individually. The corresponding fractional flow levels are summarised in Table 1 together with the computed core-averaged NWP saturation values (shown by the horizontal dashed lines in the figure). The latter are computed by considering only the central portion of the rock sample (filled symbols, $L = 20 - 59$ mm), where a uniform saturation is achieved; this region can be safely considered to be out of the reach of boundary-effects, which are are particularly evident for imbibition cycles B and C. Overall, the obtained saturation profiles show the expected behaviour with the average NWP saturation increasing (or decreasing) with increasing (or decreasing) NWP fractional flow. Because the capillary pressure is known to be an increasing function of the NWP saturation, each profile in the figure can thus be associated with the attainment of a new (average) capillary pressure equilibrium value.

The steady-state 1D NWP saturation profiles acquired during the multi-rate drainage core-flood are plotted in Figure 5 for three different flow rates ($q = 20, 30, 50$ mL/min). Because this test is conducted by injecting the NWP only ($f_{nw}^D = 1$), the saturations profiles are no longer flat, but are characterised by a negative saturation gradient. At steady-state, the effluent stream no longer contains WP and a gradient in the capillary pressure along the sample is established that corresponds to the pressure gradient imposed by the flowing NWP. It was shown experimentally that under such conditions the total pressure drop along the sample provides a direct measure of the capillary pressure at the in-

17

let boundary (Ramakrishnan and Cappiello, 1991). The pressure drop values measured in this study are plotted in the inset of the figure as a function of the average WP saturation measured at the same location by X-ray CT for the three different flow rates (circles). MICP data gathered on a sister sample are also shown (crosses), which have been converted to the $scCO_2$/water fluid pair at experimental conditions (see Section 3.1). The resulting estimate for the interfacial tension ($\gamma_{12} = 30.1 \pm 0.1$ mN/m) agrees fairly well with values reported in the literature at similar P, T conditions (34-36 mN/m) and obtained using dedicated instrumentation (Chun and Wilkinson, 1995; Chiquet et al., 2007; Georgiadis et al., 2010). We don't consider this difference as significant, having the same quantitative effect as a mere $9°$ change in the assumed contact angle for the wetting phase ($40°$ vs. $49°$). A Brooks-Corey curve is also shown in the inset of the figure (solid line) that has been obtained upon fitting Eq. 1 to the experimental capillary pressure-saturation data (MICP and core-flood). Again, the obtained parameter values ($\widetilde{P}_e = 2.83$ kPa, $\lambda = 2.10$ and $S_{w,irr} = 0.302$) are in good agreement with independent estimates reported in the literature for Berea Sandstone (Pini and Benson (2013b) and references therein) and reflect the key features of a high-permeability, homogeneous, water-wet rock.

The experimental saturation profiles are compared in Figure 5 to those predicted by a 1D mathematical model (solid lines) that is based on the differential formulation of Darcy's equation for multiphase flows and that uses the fitted $P_c^D(S)$ curve as the key input parameter. More details on the mathematical model, on its assumptions and on its numerical solution are given in Appendix A.2. Notably, at each flow rate, the agreement between experiment observations and model predictions is very good; this provides additional support to the reliability of the experimental observations (including the capillary pressure data), thereby confirming that conditions of capillary equilibrium were attained throughout the core sample.

18

5.2. Core-scale NWP trapping

NWP fractional flows ($f_{nw} = q_{nw}/q_{inj}$) are plotted in Figure 6 as a function of the average NWP saturation, S_{nw}, for the collected drainage (filled symbols) and imbibition points (empty symbols). Saturation values represent the average of measurements acquired within the central portion of the rock sample (the filled symbols in Figure 4, also reported in Table 1). The drainage points outline one single (bounding) curve; the latter is fairly steep and reaches $f_{nw} = 1$ at a relatively small NWP saturation value ($S_{nw} \approx 0.4$). This rather inefficient displacement is typical of a system characterised by a strong viscosity contrast (here, $\mu_{nw}/\mu_w \approx 0.04$). On the other hand, three distinct curves are outlined by the imbibition points, corresponding to Cycles A, B and C, and originating at three distinct average saturations, namely $S_{nw} = 0.201, 0.394$ and 0.545. These correspond to the points of flow reversal. Notably, with exception of Cycle A, the drainage curve is partly retraced during imbibition before each scanning curve breaks off the main path. Moreover, the three scanning curves terminate at three different residual NWP average saturations. The latter haven't been directly measured (because each cycle was ended prior to reaching $f_{nw} = 0$), but have been obtained from an extrapolation (dashed lines).

The obtained residual NWP average saturations are plotted in Figure 7 as a function of the corresponding turning point saturations. Residual NWP saturations obtained in this study (crosses) increase linearly with increasing initial NWP saturation; accordingly, data have been fitted with a trapping model of the form, $S_{nw,r} = CS_{nw,i}$, with $C = 0.48$ representing the trapping fraction (dashed line). Outcomes from the present study are compared to results reported in the literature for Berea Sandstone, including $scCO_2$/brine, air-brine and air-water pairs (details are given in the caption of the figure), which also tend to follow a linear behaviour (trapping coefficients provided on the diagram). The discrepancy among the data-sets shown in the figure may be attributed to experimental uncertainties, sample variability and measurement method (including the approach to $P_c = 0$). We also note that a few studies report a better fit of experimental data upon application of the Land trapping model,

19

although the observed degree of non-linearity was also rather weak (Niu et al., 2015; Akbarabadi and Piri, 2013).

5.3. Sub-Core Scale Saturations and Trapping

Snapshots of the 3D NWP saturation distribution in the central portion of the rock sample ($x = 20 - 60$ mm) are shown in Figure 8 for the three displacement cycles at various fractional flows upon attainment of steady state. The maps are reconstructed using ($3 \times 3 \times 3$) mm^3 voxels and saturations values are reported with a precision of $S_{\mathrm{nw}} \pm 0.034$. In contrast to the uniformity of the 1D (slice-averaged) saturation profiles discussed previously (Figure 4), a wide distribution of saturation values is observed within each slice that results from the presence of sub-core scale heterogeneities. In the context of multiphase flow, the latter are to be interpreted in the form of spatially resolved capillary-saturation curves ('capillary heterogeneity') that lead to the development of local saturations. Because of the characteristic layered structure of Berea Sandstone (Brooks and Corey, 1964; Tidwell and Wilson, 1999), such heterogeneities can reach significant spatial correlation lengths within a core-sample, as it can be inferred from the 3D reconstructions shown in the figure. In fact, upon closer inspection of the drainage maps, a 5-8 mm-wide lamina with consistently lower NWP saturation values can be recognised that runs parallel to the flow direction and that is inclined with respect to the vertical axis of the sample. During drainage, the effects of this structural feature become less noticeable with increasing fractional flow, f_{nw}, and practically disappear in the map of the 50 mL/min multi-rate flood; as shown in Figure 5, at this average NWP saturation level ($S_{\mathrm{nw}} \approx 0.4$) the steeper portion of the capillary pressure curve is entered: saturation is less sensitive to the value of capillary pressure and capillary heterogeneity is thus inherently less effective. Interestingly, at a given fractional flow level, f_{nw}, the strength of saturation heterogeneity in the imbibition map appears to be somewhat weaker than the corresponding drainage case and to decrease with decreasing fractional flow. This behaviour is most likely the result of two effects: first, because of the cyclic nature of the experiment

20

and the hysteretic character of the $P_c - S$ curve, more and more NWP remains trapped in the pore space of the rock, thus leading to a more uniform saturation distribution. Secondly, during imbibition the $P_c - S$ curve tends to be significantly steeper than the primary drainage curve (see also Figure 1), because of the presence of trapped NWP, thus reducing the possibility of augmenting capillary heterogeneity effects upon flow reversal. Rather, largely different turning point saturations are expected to "converge", because the steepness of an imbibition scanning curve increases with decreasing NWP turning point saturation, as discussed in the next section.

5.4. Sub-Core Scale Drainage and Imbibition Capillary Pressure Curves

Sub-core-scale capillary pressure curves are shown in Figure 9 for four voxels selected within two slices located at 33 (top diagrams) and 57 mm (bottom diagrams) from the inlet of the core sample. In each sub-plot, data acquired during drainage are represented by the empty symbols and include all cycles, while imbibition data (filled symbols) are shown for each cycle individually (Cycle A - left, Cycle B - middle, Cycle C - right). 2D maps are also shown in the figure to highlight the location of the four selected voxels (white and black circles). These maps represent capillary heterogeneity factors, α_i, that have been obtained from the scaling of the voxel capillary pressure curves measured during drainage (Eqs. 7 and 11). To facilitate comparison, voxels have been purposely selected that are characterised by an early ($\alpha_i < 1$) and a late ($\alpha_i > 1$) invasion by the NWP during drainage. As expected, the corresponding voxel capillary pressure curves are shifted with respect to the drainage core-scale curve, thus confirming the significant degree of heterogeneity at this scale. These measurements validate experimental findings on the existence of spatially varying capillary pressure curves (Pini et al., 2012; Pini and Benson, 2013a), and extend them for the first time to imbibition conditions. It can be seen in each plot, that voxel imbibition curves originating from distinct voxel drainage curves retain a consistent pattern and, most significantly, the characteristic shape of a capillary pressure curve. Notably, these mm-scale capillary pressure curves remain

21

significantly distinct from each other down to very low capillary pressure levels (0.1-0.01 kPa), thus confirming the important role of sub-core scale heterogeneity in controlling saturation distribution in porous rocks during both drainage and imbibition displacements.

Modelling results based on the Brooks-Corey $P_c(S)$ formulation are shown in Figure 9 by solid (drainage) and dashed (imbibition) curves alongside experimental observations. For drainage conditions, the capillary scaling factor, α_i, has been used as a fitting parameter to match the sub-core scale measurements, i.e. $P_{c,i}^{D}(\widehat{S}_{w}) = \widetilde{P}_{c}^{D}(\widehat{S}_{w})/\alpha_i$, where the core-average capillary pressure $\widetilde{P}_{c}^{D}$ is computed from Eq. 1. For imbibition conditions instead, the Brooks-Corey model is applied in a truly predictive manner to describe the voxel curves. In fact, $P_{c,i}^{I}(\widehat{S}_{w,m}) = \widetilde{P}_{c}^{I}(\widehat{S}_{w,m})/(\alpha_i\beta_i)$, where the core-average capillary pressure $\widetilde{P}_{c}^{I}$ is computed from Eq. 3 and β_i depends on the (measured) turning point saturation (see also Eq. 9). The agreement between experiment and model is striking, considering that in each case the very same voxel is tracked throughout the full sequence of drainage/imbibition cycles. Notably, the same coefficient ($C = 0.48$) has been applied to describe trapping at the core- and sub-core-scale, suggesting that despite the moderate textural differences at the sub-core scale, the rock behaves rather uniformly. Furthermore, these data support the use of (simple) scaling relationship at the sub-core scale, as would be expected from the Leverett J-Function relationship (Chaouche et al., 1994; Krause et al., 2013). We also note that the ability of the model to correctly describe the measured sub-core scale imbibition $P_c(S)$-curves indicates that the wetting state of the rock was preserved over the course of the experiment, in agreement with previous independent observations (Saeedi et al., 2011) and the relatively short duration of our experiment. More experiments with other rock types with e.g., more pronounced heterogeneities and different mineralogy are needed to assess the general validity of this scaling approach and conclusions.

Figure 10 shows 2D CO_2 saturation maps of the two slices just analysed during imbibition cycle B at various fractional flows and after attaining steady-state. Again, the corresponding map of capillary heterogeneity factors is shown

22

in the centre of each figure to facilitate comparison. As expected, the average NWP saturation decreases with decreasing fractional flow. The 2D maps also confirm that the spatial distribution of CO_2 within each slice correlates well with distinct features observed in the capillary scaling map. The presence of the lamina is readily visible and its effects are manifested in less NWP penetrating that region of the sample during drainage (i.e. the snapshot at the turning point). During imbibition, the same region tends to be more strongly re-wetted by water, followed by the surrounding portion of the slice.

6. Discussion

Cyclic boundary conditions are often encountered in the subsurface and give rise to hysteresis phenomena. Common examples include a fluctuating water table and its effects on soil remediation techniques, EOR methods to re-mobilise trapped NWP or the trapping of a CO_2 plume following the imbibition of the resident brine in the post-injection period of a CO_2 storage operation. Key towards the engineering design of these operations is the ability to reconcile the variability of fluid phase saturations with (i) the hysteretic nature of the capillary pressure and (ii) the inherent heterogeneity of rocks or soils. The coupling of core-flooding methods with the simultaneous imaging of flows by e.g., X-ray CT, enables such link to be established. In this study, a previously developed method for the measurement of spatially resolved drainage capillary pressure curves has been extended to the scenario where both wetting and nonwetting phases are co-injected into the porous medium, as opposed to single NWP injection (multi-rate flood) (Pini and Benson, 2013a). Besides it being the same arrangement that is used for conventional steady-state relative permeability measurements, the new approach enables capturing a much wider portion of the capillary pressure curve by including large WP saturations. The latter are associated with relatively low capillary pressure levels (just above the capillary entry pressure of the system), which, in a multi-rate displacement experiment, can possibly be achieved only by using very low injection rates. Most signifi-

23

cantly, the co-injection arrangement has enabled us in this study to investigate the imbibition process, thus providing the whole cycle of capillary pressure and, for the first time, to experimentally access spatially resolved $P_c(S)$ scanning curves for mm-subsets of the rock sample. As discussed in the following, such developments are key towards a better understanding of capillary hysteresis associated with immiscible displacements in heterogeneous porous media.

6.1. Universal drainage and imbibition capillary pressure curve

As presented above, voxel-by-voxel $P_c(S)$ curves can be constructed by linking local saturation measurements for mm-subsets of the porous medium to representative (core-averaged) capillary pressure values. The obtained population of curves is plotted in Figure 11, thus extending the analysis presented in Section 5.4 for four voxels to the whole central section of the sample (2379 voxels in total). In the figure, voxels $P_c(S)$ curves are plotted as symbols (red for drainage and blue for imbibition), while core-averaged data are shown as black solid (for drainage) and black dashed lines (for imbibition). The left- and right-hand side plots represent unscaled, $P_c^{\mathrm{D}}(S)$ and $P_c^{\mathrm{I}}(S)$, and scaled, $\Pi_c^{\mathrm{D}}(\widehat{S}_{\mathrm{w}})$ and $\Pi_c^{\mathrm{I}}(\widehat{S}_{\mathrm{w,m}})$, capillary pressure curves, respectively. Note that the latter are multiplied by the core-average capillary entry pressure $(\widetilde{P}_{\mathrm{e}})$ to retain the same units and axis-scale in the two plots. For the sake of clearer illustration, imbibition points are plotted only for Cycle B, as opposed to the drainage dataset that includes measurements from all cycles. It can be seen that at given capillary pressure values, the unscaled $P_c(S)$ curves cover a wide range of saturations. For the drainage data, the latter decreases with increasing capillary pressure from $\sim$60 to $\sim$20 saturation units (s.u.) for the range $\sim$3-6 kPa. For the imbibition data, the observed spread of saturation values is maintained to about 50 s.u. for the full range of capillary pressure values (0.2-4 kPa). We note that in both cases, the observed spread of (effective) saturation values is significantly larger than the reported uncertainty affecting readings at this fine scale ($\widehat{S}_{\mathrm{w}} \pm 0.05$ and $\widehat{S}_{\mathrm{w,m}} \pm 0.10$ for drainage and imbibition data, respectively, and voxels with dimensions $(3 \times 3 \times 3)$ mm^3). We also note that because of the larger uncertainty,

24

a minor fraction ($< 6\%$rel.) of the points that belong the imbibition dataset fall outside the physical bound for saturation values ($\widehat{S}_{w,m} > 1$). On the right-hand plot, the same data are plotted after scaling them using Eqs. 8 and 9. It can be seen that despite its simplicity, the adopted scaling approach is quite effective, as the data now nicely gather around the two bounding capillary pressure curves. This observation is supported by the value of the minimisation function (Eq.11), which is reduced to 24% of the original (unscaled) value ($\Phi_{unsc} = 177$ vs. $\Phi_{sc} = 43$ using a total of 19,032 $P_c - S$ pairs). In practice, this result indicates that, for this sandstone, voxels can be considered *similar* in terms of pore-size distribution index, λ. While these results confirm quantitatively previous observations on a different Berea Sandstone sample (Pini and Benson, 2013a), this is the first time that the approach is extended to and validated for imbibition conditions. In particular, we note that the scaling of imbibition capillary pressure curves did not require the introduction (i.e. fitting) of additional parameters, because the value of the trapping coefficient C measured at the core-scale has been applied also at the sub-core scale. Because trapping is ultimately controlled by the microscopic pore-space geometry, this result is consistent with the similarity criterion discussed above. As such, these observations suggest that knowledge of λ and of the scaling factors α_i may be sufficient to describe the pertinent microscopic properties of Berea Sandstone, even when hysteresis is involved. This further promotes Berea Sandstone as an excellent candidate for benchmarking displacements governed by imbibition in heterogeneous media beyond the application of the geological storage of CO_2, such as for a systematic evaluation of water-flooding techniques for enhanced oil recovery.

6.2. Capillary heterogeneity

The capillary scaling factors, α_i, obtained from the scaling of sub-core scale capillary pressure curves can be used to represent the heterogeneity of the system under study in 3D, as shown in Figure 12a. Notably, the same voxels that reported a late filling by the NWP in the saturation maps shown in Figure 8 are now parameterised through a small scaling factor ($\alpha_i < 1$), i.e., at

these specific locations a larger capillary pressure is required to reach the same saturation as the core-averaged value. In agreement with published results on another sample of the same rock type (but with significantly different average permeability) (Pini and Benson, 2013a), the obtained values of the scaling factors deviate up to 15% from the mean for $(3 \times 3 \times 3)\text{mm}^3$ voxels. When the $P_\text{c} - S$ curve is described by the Brooks-Corey model, the scaling factors reduce to the ratio between core- and the sub-core-scale capillary entry pressure values (Eq.7) and allow estimating a dimensionless heterogeneity number, $\eta = \texttt{std}(P_{\text{e},i})/\texttt{mean}(P_{\text{e},i})$ (Li and Benson, 2015). The latter is a measure of the strength of capillary heterogeneity in the rock and takes the value $\eta \approx 0.1$ for the sandstone considered in this study. For comparison purposes, a value of $\eta \approx 0.4$ was adopted to study upward CO_2 migration in a uniformly heterogeneous meter-scale domain using highly-resolved numerical simulations (Li and Benson, 2015). Results from the model indicated that when mm-scale heterogeneities are accounted for, (i) the CO_2 frontal speed is significantly reduced (up to a factor of two) and (ii) the plume can be completely immobilised for a condition of limited CO_2 supply. Remarkably, both observations have been recently confirmed through direct experimental observations in a meter-scale sand-packed aquifer tank (Trevisan et al., 2017). The key message here is that the effects of small-scale heterogeneities can propagate to much larger observational scales (in the order of meters) for fluid migration that is primarily driven by buoyancy and capillarity. The experimental approach presented in this study is an effective method for the parameterisation of such small-scale heterogeneities in rock cores, whose knowledge is needed for correctly designing and interpreting core-scale measurements of e.g., relative permeability curves (Reynolds and Krevor, 2015). As shown in a previous study (Pini and Benson, 2013a), the obtained scaling factors can also be used to estimate sub-core scale permeability values. We will demonstrate in the following that the obtained parameterisation is close agreement with independent experimental observations.

6.3. Permeability heterogeneity

The remaining 3D maps shown in Figure 12 include porosity (b) and permeability (c)-(d). Porosity is regarded as the primary variable measurable from X-ray based imaging techniques (Pini and Madonna, 2016), because it relies solely on the subtraction of two sets of scans (of the dry- and a water-saturated

720 sample). As expected and shown in the 3D map, porosity in Berea Sandstone is relatively uniform and presents only modest strength of variability ($21.5-23.5\%$, corresponding to deviations of about 4%rel. from the mean). For this reason, other petrophysical properties, such as the permeability, are deemed as more appropriate for the characterisation of heterogeneity. As shown in map (d), sub-

725 core scale permeability can be estimated based solely on porosity distribution using the Kozeny-Carman relationship or variations thereof (Shi et al., 2011; Krause et al., 2013). While the strength of heterogeneity is now significantly enhanced (about 20%rel.), the spatial distribution of high and low permeability regions closely mimic the pattern observed for the porosity. Notably, studies

730 based on numerical simulations have consistently shown that such sub-core scale permeability maps fail to provide the required input to enable a satisfactory match between predicted sub-core scale saturation distribution and experimental observations at the same scale (Krause et al., 2013; Kuo and Benson, 2015). As such, it comes as no surprise that no clear correlation can be found between

735 map (b) or (d) and the saturation maps presented in Figure 8. Supported by earlier experimental observations (Chaouche et al., 1994), the same numerical studies propose to compute sub-core scale permeability based on capillary pressure through the well-known *J*-Leverett scaling relationship (Leverett, 1941), $J(S) = \sqrt{k/\phi}P_\mathrm{c}(S)/\gamma$. The latter represents a special case of the universal cap-

740 illary pressure curve developed in this study, Eq.(8), and expresses the scaling factor in terms of fluid and rock properties. Hence, voxel permeability values can be readily estimated from the capillary scaling factors as $k_i = \alpha_i^2 \widetilde{k}\phi_i/\widetilde{\phi}$, where $\widetilde{k}$ and $\widetilde{\phi}$ are core-averaged permeability and porosity (Pini and Benson, 2013a). The corresponding 3D reconstruction for the sample investigated in

745 this study is shown in Figure 12c in terms of a normalised permeability, $k_i/\widetilde{k}$.

27

We note that the obtained permeability map is now characterised by a low-permeability lamina that is oriented sub-parallel to the axis of the core. The latter is reminiscent of the finer-textured strata that are often observed in Berea Sandstone cores (Brooks and Corey, 1964; Tidwell and Wilson, 1999) and can be directly correlated to the distinctive features of the saturation distributions shown in Figure 8.

The normal probability plot of log-permeability values obtained through the capillary-based approach (empty symbols) and the Kozeny-Carman model (filled symbols) is shown in Figure 13 alongside theoretical distributions with variances $\sigma_{\ln k}^2 = 0.01 - 4$. With reference to numerical studies that have addressed geological sequestration of CO_2, the latter cover the range from moderate ($\sigma_{\ln k}^2 = 0.3 - 0.7$, Lengler et al. (2010); Deng et al. (2012); Li and Benson (2015)) to highly heterogeneous systems ($\sigma_{\ln k}^2 = 1 - 4$, Saadatpoor et al. (2010); Cameron and Durlofsky (2012); Rabinovich et al. (2015); Trevisan et al. (2017)). It can be seen that the two experimental data sets form two distinct straight lines and are therefore log-normally distributed. However, the obtained strength of heterogeneity is quite different, with the capillary-based approach producing a more heterogeneous distribution ($\sigma_{\ln k}^2 = 0.032$) than the Kozeny-Carman model ($\sigma_{\ln k}^2 = 0.009$). Most significantly, we show here that the strength of permeability heterogeneity produced by the capillary-based approach agrees well with independent measurements on Berea Sandstone from mini-permeameter tests carried out at the same scale (dashed-lines, $\sigma_{\ln k}^2 = 0.021 - 0.046$, for tip seals $1.5 - 3.1$ mm in size) (Tidwell and Wilson, 1999). This validation is important, because it indicates that accurate parameterisation of rock properties at the sub-core scale can be achieved non-invasively in terms of both multiphase (capillary scaling factor) and petrophysical properties (porosity, permeability). In addition to being quantitative indicators of heterogeneity, sub-core scale properties can be used to populate numerical models, which in turn can be used to validate observations from single- (Pini et al., 2016) and two-phase core-flooding experiments (Krause et al., 2013). We contend that this approach is very valuable, if not necessary, for the development of reliable simulation tools that allow

28

extending these experiments to conditions (e.g., flow rates) that are prevalent in the subsurface, which would be otherwise not easily attainable in the laboratory.

7. Concluding remarks

We have presented results from a detailed experimental investigation on capillary pressure heterogeneity and hysteresis for the $scCO_2$/water system on Berea Sandstone enabled by 3D X-ray CT imagery at mm-resolution. A core-analysis workflow is proposed that uses capillary scaling as the mean for accurate parameterisation of capillary heterogeneity and other key petrophysical properties, such as the permeability, at the sub-core scale. The description of rock heterogeneity can thus be greatly simplified and reduced to two separate universal capillary scaling curves (for drainage and imbibition), and a set of spatially distributed capillary scaling factors. As such, this approach is very valuable for core-analysis practitioners, as it provides a practical way to compare samples and rock types, and to obtain input parameters for numerical simulators to examine flow conditions that are difficult to achieve experimentally. In Berea Sandstone, permeability heterogeneity at the sub-core scale ($\sim$0.027 cm^3 vs. $\sim$200 cm^3 representing the core-scale) is significant ($\sigma^2_{\ln k} = 0.032$) and stronger than what would be predicted based on the Kozeny-Carman model ($\sigma^2_{\ln k} = 0.009$) at the same scale. Our experimental observations shed light on a fundamental issue associated with multiphase flow in porous media, that is, the role of these sub-core scale heterogeneities in controlling nonwetting phase trapping during imbibition. In fact, while for drainage displacements the importance of capillary heterogeneity is now widely acknowledged, we provide direct experimental evidence here that it is (at least) as important in controlling local saturation development during imbibition. While they are limited in this study to one rock type/one sample, these observations highlight the importance of extending the current experimental data set associated with imbibition conditions to more rock types and fluid pairs, as these are not only prevailing in the post-injection phase of a CO_2 storage operation, but also in commonly adopted

29

strategies for enhanced oil recovery operations.

Acknowledgements

810 ## Appendix

A.1. Trapping model

We follow here the approach reported by Land (Land, 1968), and subsequently adopted by others (Lake, 1996), where it is assumed that at any given capillary pressure value, the saturation configurations of connected NWP that
815 correspond to the drainage and imbibition branches of the $P_c(S)$ curve are identical. That is, the fraction of NWP that remains mobile during an imbibition event $(\widehat{S}_{\mathrm{nw,m}})$ can be associated to the same pore sizes occupied by the NWP during a drainage process, i.e. where $\widehat{S}_{\mathrm{nw}} = \widehat{S}_{\mathrm{nw,m}}$ always. The fraction of NWP that remains trapped along an imbibition event $(\widehat{S}_{\mathrm{nw,t}})$ is thus obtained
820 from a simple material balance:

$$\widehat{S}_{\mathrm{nw,t}} = \widehat{S}_{\mathrm{nw}} - \widehat{S}_{\mathrm{nw,m}} \qquad \text{(A-1)}$$

where $\widehat{S}_{\mathrm{nw}}$ is the total NWP saturation. Note that *trapped* differs from *residual* saturation: the former is associated to any capillary pressure value, while the latter refers to the termination of an imbibition curve, which, for a strongly wetted system, corresponds to the disappearance of a continuous gas
825 phase - which occurs when the continuum scale capillary pressure goes to zero. It is also generally acknowledged (Lake, 1996) that residual saturations depend on the corresponding saturation at the point of flow reversal, i.e. $\widehat{S}_{\mathrm{nw,r}} = f(\widehat{S}_{\mathrm{nw,i}})$, and that this relationship is a fingerprint of a given rock type, just as is the capillary pressure curve. Two of the most popular NWP trapping models are
830 the linear (Ruprecht et al., 2014), $\widehat{S}_{\mathrm{nw,r}} = C\widehat{S}_{\mathrm{nw,i}}$, and the Land model (Land,

30

1968), $\widehat{S}_{\mathrm{nw,r}} = \widehat{S}_{\mathrm{nw,i}}/(1 + C_{\mathrm{L}}\widehat{S}_{\mathrm{nw,i}})$. Thus, given an initial saturation, $\widehat{S}_{\mathrm{nw,i}}$, the corresponding trapped saturation can be calculated as follows:

$$\widehat{S}_{\mathrm{nw,t}} = \widehat{S}_{\mathrm{nw,r}}(\widehat{S}_{\mathrm{nw,i}}) - \widehat{S}_{\mathrm{nw,r}}(\widehat{S}_{\mathrm{nw,m}}) \tag{A-2}$$

that is, the amount of NWP that is currently trapped equals the difference between the (residual) amount that may ultimately be trapped (computed from the maximum historical NWP saturation) and the amount yet to be trapped (computed from the current mobile NWP fraction). Closed-form expressions for the mobile NWP saturation can be obtained upon combination of either one of the two trapping models with Eqs. A-1 and A-2, thus leading to the equations provided in the manuscript text, i.e. Eqs. 5 and 6.

A.2. 1D model for simulating multi-rate drainage core-floods

At steady-state, the one-dimensional form of Darcy's equation extended to multiphase flow reads as follows,

$$q = -\frac{Akk_{\mathrm{r,nw}}(S_{\mathrm{w}})}{\mu_{\mathrm{nw}}}\frac{dP_{\mathrm{c}}(S_{\mathrm{w}})}{dx} \tag{A-3}$$

where q is the volumetric flow rate, A is the sample's cross section, k is its permeability, $k_{\mathrm{r,nw}}$ is the drainage relative permeability to the NWP, μ_{nw} its viscosity, P_{c} is the capillary pressure and x is the distance from the inlet face of the core. Note that Eq. A-3 assumes that (i) the NWP behaves as an incompressible fluid (and thus the flow rate q at any location in the core equals the injection value, q_{inj}) and that (ii) the permeability is constant throughout the core. The first assumption is justified, because at the flow rates considered here (20-50 mL/min) the measured pressure drop is always < 10 kPa; the latter affects q by less than 1% at the applied experimental conditions (9 MPa pore pressure and temperature of 50°C). The second assumption is supported by the known uniformity of Berea Sandstone at the core scale. Thus, Eq. A-3 can be

31

rearranged as follows:

$$\frac{dS_{\mathrm{w}}}{dx_{\mathrm{D}}} = \left(\frac{q_{\mathrm{inj}}\mu_{\mathrm{nw}}L}{Ak}\right)\left(\frac{1}{k_{\mathrm{r,nw}}(S_{\mathrm{w}})}\right)\left(\frac{1}{dP_{\mathrm{c}}/dS_{\mathrm{w}}}\right) \qquad \text{(A-4)}$$

with $x_{\mathrm{D}} = 1 - x/L$ and where the chain rule has been applied to the term $dP_{\mathrm{c}}/dx_{\mathrm{D}}$, i.e.

$$\frac{dP_{\mathrm{c}}}{dx_{\mathrm{D}}} = \frac{dP_{\mathrm{c}}}{dS_{\mathrm{w}}} \cdot \frac{dS_{\mathrm{w}}}{dx_{\mathrm{D}}} \qquad \text{(A-5)}$$

Constitutive relationships for capillary pressure and relative permeability curves are needed to solve Eq. A-4. In this study, the Brooks-Corey model (Eq. 1, fitted to experimental data) is used to describe the former, which is then used within the framework of Burdine's theory to calculate the nonwetting relative permeability drainage curve (Brooks and Corey, 1964):

$$k_{\mathrm{r,nw}} = (1 - \widehat{S}_{\mathrm{w}})^2 \left[1 - \widehat{S}_{\mathrm{w}}^{(2+\lambda)/\lambda}\right] \qquad \text{(A-6)}$$

where $\widehat{S}_{\mathrm{w}}$ is given by Eq. 2. Note that no additional parameters are introduced in Eq. A-6, which will therefore be applied in a fully predictive way. The derivative of the capillary pressure required for the third term in Eq. A-4 is given by

$$\frac{dP_{\mathrm{c}}}{dS_{\mathrm{w}}} = -\frac{P_{\mathrm{e}}}{\lambda(1 - S_{\mathrm{w,ir}})}\widehat{S}_{\mathrm{w}}^{-\left(\frac{1+\lambda}{\lambda}\right)} \qquad \text{(A-7)}$$

Eq. A-4 (together with Eqs. A-6 and A-7) is solved to predict saturation profiles along the length of the core using the `ode45` solver in MATLAB by providing appropriate initial conditions, namely $S_{\mathrm{w}}(x_{\mathrm{D}} = 0) = S_{\mathrm{w}}(x = L)$, which can be readily obtained by X-ray CT measurements.

References

Akbarabadi, M., Piri, M., 2013. Relative permeability hysteresis and capillary trapping characteristics of supercritical CO_2/brine systems: An experimental study at reservoir conditions. Adv. Water Res. 52, 190–206.

Al-Menhali, A., Niu, B., Krevor, S., 2015. Capillarity and wetting of carbon dioxide and brine during drainage in Berea Sandstone at reservoir conditions. Water Resour. Res. 51, 7895–7914.

Alemu, B.L., Aker, E., Soldal, M., Johnsen, Ø., Aagaard, P., 2013. Effect of sub-core scale heterogeneities on acoustic and electrical properties of a reservoir rock: a CO_2 flooding experiment of brine saturated sandstone in a computed tomography scanner. Geophys. Prospect. 61, 235–250.

Anderson, W., 1987. Wettability literature survey - Part 4: Effects of wettability on capillary pressure. J. Petrol. Technol. 39, 1283–1300.

Andrew, M., Bijeljic, B., Blunt, M.J., 2014. Pore-scale contact angle measurements at reservoir conditions using X-ray microtomography. Adv. Water Res. 68, 24–31.

Blunt, M., Fayers, F.J., Orr, F.M., 1993. Carbon dioxide in enhanced oil recovery. Energ. Convers. Manage. 34, 1197–1204.

Brooks, R.H., Corey, A.T., 1964. Hydraulic properties of porous media. Hydrology Paper No. 3, Colorado State University , 1–27.

Cameron, D.A., Durlofsky, L.J., 2012. Optimization of well placement, CO_2 injection rates, and brine cycling for geological carbon sequestration. Int. J. Greenhouse Gas Control 10, 100–112.

Chaouche, M., Rakotomalala, N., Salin, D., Xu, B., Yortsos, Y., 1994. Capillary effects in drainage in heterogeneous porous media: continuum modelling, experiments and pore network simulations. Chem. Eng. Sci. 49, 2447–2466.

Chiquet, P., Daridon, J.L., Broseta, D., Thibeau, S., 2007. CO_2/water interfacial tensions under pressure and temperature conditions of CO_2 geological storage. Energ. Convers. Manage. 48, 736–744.

Chun, B.S., Wilkinson, G.T., 1995. Interfacial tension in high-pressure carbon dioxide mixtures. Ind. Eng. Chem. Res. 34, 4371–4377.

33

Crowell, D.C., Dean, G.W., Loomis, A.G., 1966. Efficiency of gas displacement from a water-drive reservoir. volume 6735. US Dept. of the Interior, Bureau of Mines.

Deng, H., Stauffer, P.H., Dai, Z., Jiao, Z., Surdam, R.C., 2012. Simulation of industrial-scale CO_2 storage: Multi-scale heterogeneity and its impacts on storage capacity, injectivity and leakage. Int. J. Greenhouse Gas Control 10, 397–418.

Doughty, C., 2007. Modeling geologic storage of carbon dioxide: comparison of non-hysteretic and hysteretic characteristic curves. Energ. Convers. Manage. 48, 1768–1781.

Egermann, P., Lenormand, R., 2005. A new methodology to evaluate the impact of localized heterogeneity on petrophysical parameters (k_r, P_c) applied to carbonate rocks. Petrophysics 46, 335–345.

El-Maghraby, R.M., Blunt, M.J., 2012. Residual CO_2 trapping in Indiana limestone. Environ. Sci. Technol. 47, 227–233.

Ganapathy, S., Wreath, D.G., Lim, M.T., Rouse, B.A., Pope, G.A., Sepehrnoori, K., 1993. Simulation of heterogeneous sandstone experiments characterized using CT scanning. SPE Formation Eval. 8, 273–279.

Georgiadis, A., Maitland, G., Trusler, J.P.M., Bismarck, A., 2010. Interfacial tension measurements of the (H_2O + CO_2) system at elevated pressures and temperatures. J. Chem. Eng. Data 55, 4168–4175.

Graue, A., 1994. Imaging the effects of capillary heterogeneities on local saturation development in long corefloods. SPE Drill. Completion 9, 57–64.

Haines, W.B., 1930. Studies in the physical properties of soil. V. The hysteresis effect in capillary properties, and the modes of moisture distribution associated therewith. J. Agr. Sci. 20, 97–116.

Huang, Y., Ringrose, P., Sorbie, K., 1995. Capillary trapping mechanisms in water-wet laminated rocks. SPE Res. Eng. 10, 287–292.

Ide, S.T., Jessen, K., Orr, F.M., 2007. Storage of CO_2 in saline aquifers: Effects of gravity, viscous, and capillary forces on amount and timing of trapping. Int. J. Greenhouse Gas Control 1, 481–491.

IPCC, 2005. IPCC Special Report on Carbon Dioxide Capture and Storage. Prepared by Working Group III of the Intergovernmental Panel on Climate Change. [Metz, B., O. Davidson, H. C. de Coninck, M. Loos, and L. A. Meyer (eds.)]. Cambridge University Press, Cambridge, United Kingdom and New York, NY, USA.

Juanes, R., Spiteri, E., Orr, F., Blunt, M., 2006. Impact of relative permeability hysteresis on geological CO_2 storage. Water Resour. Res. 42, W12418.

Kovscek, A., Cakici, M., 2005. Geologic storage of carbon dioxide and enhanced oil recovery. II. Co−optimization of storage and recovery. Energ. Convers. Manage. 46, 1941–1956.

Krause, M., Krevor, S., Benson, S.M., 2013. A procedure for the accurate determination of sub-core scale permeability distributions with error quantification. Transport Porous Med. 98, 565–588.

Krevor, S., Blunt, M.J., Benson, S.M., Pentland, C.H., Reynolds, C., Al-Menhali, A., Niu, B., 2015. Capillary trapping for geologic carbon dioxide storage–from pore scale physics to field scale implications. Int. J. Greenhouse Gas Control 40, 221–237.

Krevor, S., Pini, R., Li, B., Benson, S.M., 2011. Capillary heterogeneity trapping of CO_2 in a sandstone rock at reservoir conditions. Geophys. Res. Lett. 38.

Krevor, S., Pini, R., Zuo, L., Benson, S.M., 2012. Multiphase flow properties of CO_2 and water in sandstone rocks at reservoir conditions. Water Resour. Res. 48.

Kuo, C.W., Benson, S.M., 2015. Numerical and analytical study of effects of small scale heterogeneity on CO_2/brine multiphase flow system in horizontal corefloods. Adv. Water Res. 79, 1–17.

Lake, L.W., 1996. Enhanced Oil Recovery. Prentice Hall.

Land, C.S., 1968. Calculation of imbibition relative permeability for two-and three-phase flow from rock properties. Soc. Petrol. Eng. J. 8, 149–156.

Lehmann, P., Stauffer, F., Hinz, C., Dury, O., Flühler, H., 1998. Effect of hysteresis on water flow in a sand column with a fluctuating capillary fringe. J. Contam. Hydrol. 33, 81–100.

Lengler, U., De Lucia, M., Kühn, M., 2010. The impact of heterogeneity on the distribution of CO_2: numerical simulation of CO_2 storage at Ketzin. Int. J. Greenhouse Gas Control 4, 1016–1025.

Lenormand, R., Eisenzimmer, A., Zarcone, C., 1993. A novel method for the determination of water/oil capillary pressures of mixed-wettability samples. Soc. Core Analyst Conf. Paper 9322, 1–15.

Leverett, M.C., 1941. Capillary behavior in porous solids. Petrol. Trans. AIME 142, 152–169.

Li, B., Benson, S.M., 2015. Influence of small-scale heterogeneity on upward CO_2 plume migration in storage aquifers. Adv. Water Res. 83, 389–404.

Li, X., Akbarabadi, M., Karpyn, Z.T., Piri, M., Bazilevskaya, E., 2015. Experimental investigation of carbon dioxide trapping due to capillary retention in saline aquifers. Geofluids 15, 563–576.

Li, K., Horne, R.N., 2001. An experimental and analytical study of steam/water capillary pressure. SPE Res. Eval. Eng. 4, 477–482.

Miller, E., Miller, R., 1956. Physical theory for capillary flow phenomena. J. Appl. Phys. 27, 324–332.

Morrow, N.R., Harris, C.C., 1965. Capillary equilibrium in porous materials. Soc. Petrol. Eng. J. 5, 15–24.

Niu, B., Al-Menhali, A., Krevor, S., 2015. The impact of reservoir conditions on the residual trapping of carbon dioxide in berea sandstone. Water Resour. Res. 51, 2009–2029.

Oh, J., Kim, K., Han, W.S., Park, E., Kim, J., 2015. Migration behavior of supercritical and liquid CO_2 in a stratified system: Experiments and numerical simulations. Water Resour. Res. 51, 7937–7958.

Oh, J., Kim, K.Y., Han, W.S., Kim, T., Kim, J.C., Park, E., 2013. Experimental and numerical study on supercritical CO_2/brine transport in a fractured rock: Implications of mass transfer, capillary pressure and storage capacity. Adv. Water Res. 62, 442–453.

Ott, H., Pentland, C., Oedai, S., 2015. CO_2–brine displacement in heterogeneous carbonates. Int. J. Greenhouse Gas Control 33, 135–144.

Pentland, C.H., El-Maghraby, R., Iglauer, S., Blunt, M.J., 2011. Measurements of the capillary trapping of supercritical carbon dioxide in Berea Sandstone. Geophys. Res. Lett. 38, L06401.

Perrin, J.C., Benson, S.M., 2010. An experimental study on the influence of sub-core scale heterogeneities on CO_2 distribution in reservoir rocks. Transport Porous Med. 82, 93–109.

Pini, R., Benson, S.M., 2013a. Characterization and scaling of mesoscale heterogeneities in sandstones. Geophys. Res. Lett. 40, 3903–3908.

Pini, R., Benson, S.M., 2013b. Simultaneous determination of capillary pressure and relative permeability curves from coreflooding experiments with various fluid pairs. Water Resour. Res. 49, 3516–3530.

Pini, R., Krevor, S., Benson, S.M., 2012. Capillary pressure and heterogeneity for the CO_2/water system in sandstone rocks at reservoir conditions. Adv. Water Res. 38, 48–59.

37

Pini, R., Madonna, C., 2016. Moving across scales: a quantitative assessment of X-ray CT to measure the porosity of rocks. J. Porous Mat. 23, 325–338.

Pini, R., Vandehey, N.T., Druhan, J., O'Neil, J.P., Benson, S.M., 2016. Quantifying solute spreading and mixing in reservoir rocks using 3-D PET imaging. J. Fluid Mech. 796, 558–587.

Plug, W.J., Bruining, J., 2007. Capillary pressure for the sand–CO_2–water system under various pressure conditions. application to CO_2 sequestration. Adv. Water Res. 30, 2339–2353.

Purcell, W.R., 1949. Capillary pressures−Their measurement using mercury and the calculation of permeability therefrom. J. Pet. Technol. 1, 39–48.

Qi, R., LaForce, T.C., Blunt, M.J., 2009. Design of carbon dioxide storage in aquifers. Int. J. Greenhouse Gas Control 3, 195–205.

Rabinovich, A., Itthisawatpan, K., Durlofsky, L.J., 2015. Upscaling of CO_2 injection into brine with capillary heterogeneity effects. J. Petrol. Sci. Eng. 134, 60–75.

Raeesi, B., Morrow, N.R., Mason, G., 2014. Capillary pressure hysteresis behavior of three sandstones measured with a multistep outflow–inflow apparatus. Vadose Zone J. 13, 1–12.

Ramakrishnan, T., Cappiello, A., 1991. A new technique to measure static and dynamic properties of a partially saturated porous medium. Chem. Eng. Sci. 46, 1157–1163.

Reynolds, C., Krevor, S., 2015. Characterizing flow behavior for gas injection: Relative permeability of CO_2−brine and N_2−water in heterogeneous rocks. Water Resour. Res. 51, 9464–9489.

Ringrose, P., Sorbie, K., Corbett, P., Jensen, J., 1993. Immiscible flow behaviour in laminated and cross-bedded sandstones. J. Petrol. Sci. Eng. 9, 103–124.

Ruprecht, C., Pini, R., Falta, R., Benson, S., Murdoch, L., 2014. Hysteretic trapping and relative permeability of CO_2 in sandstone at reservoir conditions. Int. J. Greenhouse Gas Control 27, 15–27.

Saadatpoor, E., Bryant, S.L., Sepehrnoori, K., 2010. New trapping mechanism in carbon sequestration. Transp. Porous Media 82, 3–17.

Saeedi, A., Rezaee, R., Evans, B., Clennel, B., 2011. Multiphase flow behaviour during CO_2 geo-sequestration: Emphasis on the effect of cyclic CO_2-brine flooding. J. Petr. Sci. Eng. 79, 65–85.

Shafer, J., 2013. Recent advances in core analysis. Petrophysics 54, 554–579.

Shi, J.Q., Xue, Z., Durucan, S., 2011. Supercritical CO_2 core flooding and imbibition in tako sandstone-influence of sub-core scale heterogeneity. Int. J. Greenhouse Gas Control 5, 75–87.

Tidwell, V.C., Wilson, J.L., 1999. Permeability upscaling measured on a block of Berea Sandstone: Results and interpretation. Math. Geol. 31, 749–769.

Tokunaga, T.K., Wan, J., Jung, J., Kim, T.W., Kim, Y., Dong, W., 2013. Capillary pressure and saturation relations for supercritical CO_2 and brine in sand: Highpressure $P_c(S_w)$ controller/meter measurements and capillary scaling predictions. Water Resour. Res. 49, 4566–4579.

Trevisan, L., Pini, R., Cihan, A., Birkholzer, J.T., Zhou, Q., GonzálezNicolás, A., Illangasekare, T.H., 2017. Imaging and quantification of spreading and trapping of carbon dioxide in saline aquifers using meterscale laboratory experiments. Water Resour. Res. in press.

Wang, S., Tokunaga, T.K., 2015. Capillary pressure-saturation relations for supercritical CO_2 and brine in limestone/dolomite sands: Implications for geologic carbon sequestration in carbonate reservoirs. Environ. Sci. Technol. 49, 7208–7217.

39

1060 Wilkinson, D., 1996. Percolation effects in immiscible displacement. Phys. Rev.
        A 34, 1380–1391.

Tables

f_{nw}^A	S_{nw}^A	P_c^A	0.30	0.212	0.264
0.50	0.097	3.04	0.00	0.197^a	-
0.80	0.201	3.33			
0.70	0.180	2.51	f_{nw}^C	S_{nw}^C	P_c^C
0.58	0.162	1.88	0.85	0.258	3.52
0.47	0.150	1.49	0.95	0.318	3.78
0.25	0.134	1.00	0.995	0.413	4.33
0.00	0.117^a	-	1.00	*0.484*	*4.97*
			1.00^b	*0.516*	*5.36*
f_{nw}^B	S_{nw}^B	P_c^B	1.00^c	*0.545*	*5.82*
0.93	0.282	3.62	0.97	0.336	0.625
0.99	0.394	4.20	0.90	0.299	0.283
0.97	0.349	2.76	0.50	0.267	0.0297
0.94	0.289	1.43	0.05	0.263	0.0004
0.88	0.261	0.952	0.00	0.258^a	-
0.70	0.239	0.623			

Table 1: Experimental fractional flows (f_{nw}^i), measured NWP saturation (S_{nw}^i) and computed capillary pressure data (P_c^i [kPa]) for the sequence of three drainage/imbibition cycles (i =A, B, C). Experimental conditions were: $T = 50°$C, $P = 9$ MPa. Saturation values represent the average of measurements acquired within the central portion of the rock sample ($L = 20 - 60$ mm, corresponding to the filled symbols in Figure 4), with the exception of those reported in *italic*, which refer to $L = 20$ mm only (inlet). Capillary pressure data are computed accordingly. [a]Residual saturation obtained from an extrapolation to $P_c^i = 0$;. [b]$q = 30$ mL/min. [c]$q = 50$ mL/min.

Figures
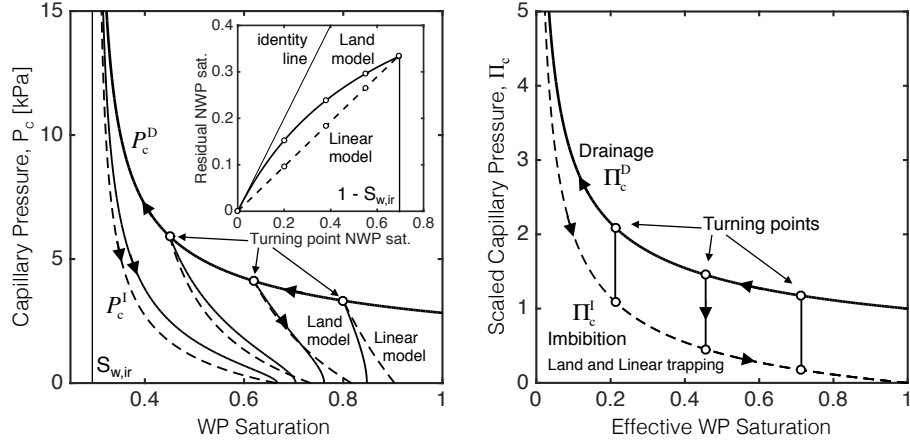
Figure 1: Capillary pressure hysteretic model: *left* - bounding drainage and scanning imbibition curves are constructed using the Brooks-Corey formalism (Eqs. 1 and 3), with the following model parameters: $P_e = 2.83$ kPa, $\lambda = 2.1$, $S_{w,ir} = 0.302$. Trapping during imbibition is described through either a linear relationship ($C = 0.48$, dashed lines) or the Land model ($C_L = 1.09$, solid lines), as shown in the inset of the figure. Scanning curves are assumed to be fully reversible; *right* - universal drainage and imbibition capillary pressure curves, as obtained from Eqs. 8 and 9.
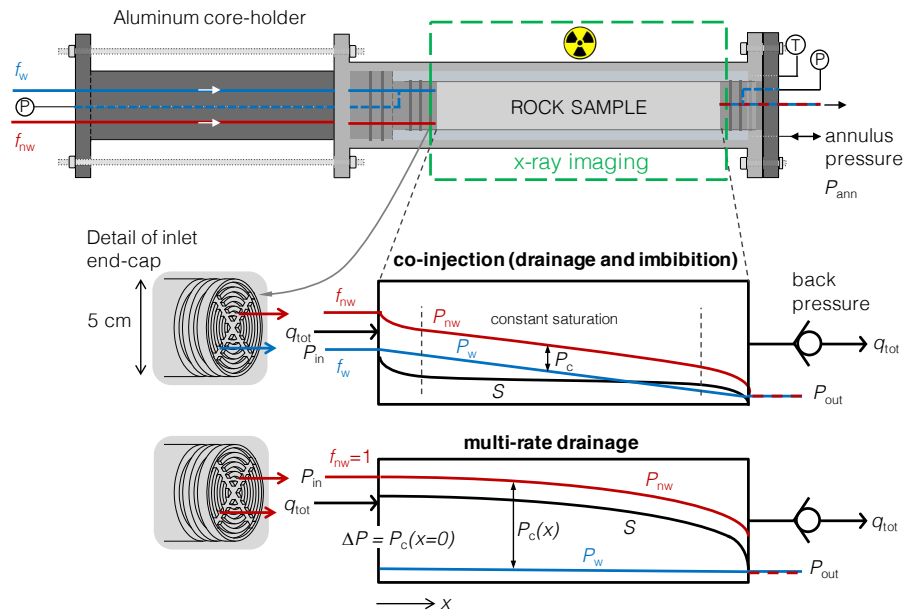
Figure 2: Schematic representation of the high-pressure core-holder and of the two approaches adopted in this study for measuring a capillary pressure curve (i) from a multi-rate core-flood (NWP injection) and (ii) for a situation where both NWP and WP are co-injected (drainage and imbibition). The diagrams represent the expected steady-state NWP saturation profiles (black lines) in the rock sample (obtained from X-ray CT imaging), together with the corresponding pressure profiles (coloured lines). Note that NWP and WP are injected through separate tubings ported directly to the inlet face of the sample and the inlet pressure is measured in the WP line only. During the multi-rate drainage test, both ports are used for NWP injection.
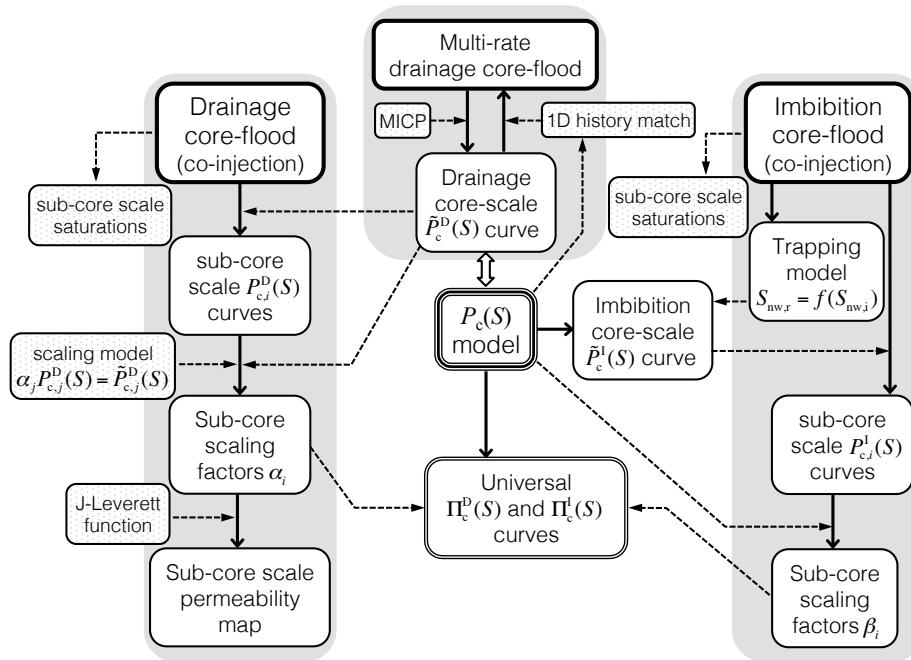
Figure 3: Core-analysis workflow for the determination of core- and sub-core scale capillary pressure curves, and for the parameterisation of rock properties at the sub-core scale through scaling functions.
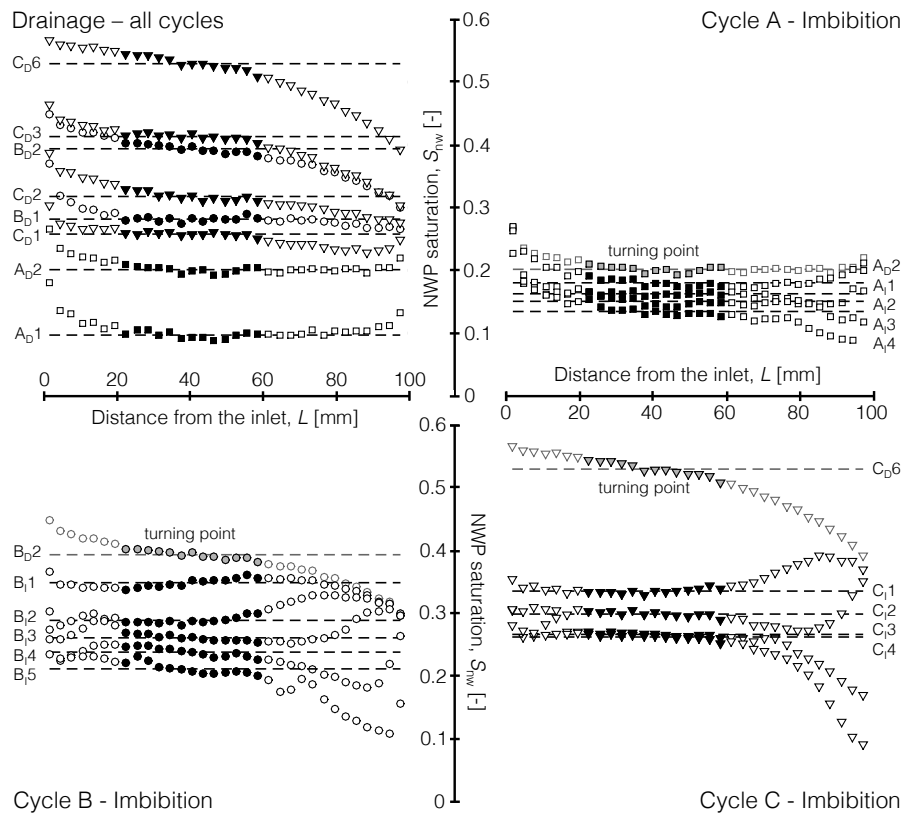
Figure 4: Steady-state 1D (slice-averaged) NWP saturation profiles along the length of the rock sample at various fractional flows. Data acquired during drainage steps are shown in the top-left corner, while those obtained during imbibition steps are shown in the remaining quandrants for each cycle individually. The filled symbols highlight the portion of the rock used for subsequent analysis. Each curve is labelled as $X_Y N$, where X represents the cycle, Y the type of displacement (D for drainage and I for imbibition), and N the step within the cycle.

45
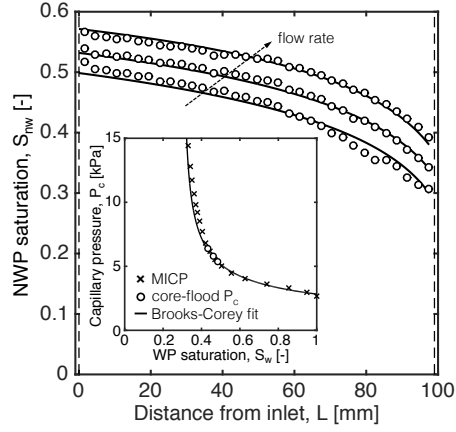
Figure 5: Steady-state 1D (slice-averaged) NWP saturation profiles along the length of the rock sample acquired during a multi-rate flood with $f_{nw} = 1$ and $q = 20, 30, 50$ mL/min. Symbols represent in-situ measurements by X-ray CT scanning, while the solid lines are predictions from the 1D model described in Appendix A.2 that uses the capillary pressure-saturation curve shown in the inset. The latter is constructed based on direct core-flooding measurements (circles) and converted MICP data (crosses, with $\gamma_{12} = 30$ mN/m, $\gamma_{HgA} = 485$ mN/m). A Brooks-Corey model fit to the measured capillary pressure data is also shown (Eq. 1 with $\widetilde{P}_e = 2.83$ kPa, $\lambda = 2.10$ and $S_{w,irr} = 0.302$).
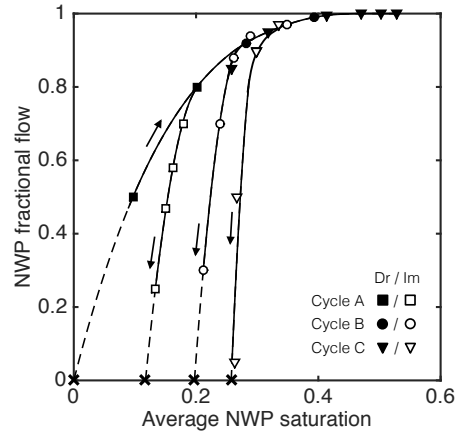
Figure 6: NWP fractional flow (f_{nw}) as a function of the steady-state core-averaged NWP saturation (S_{nw}) measured during the sequence of drainage (filled symbols) and imbibition (empty symbols) displacements. Saturation values represent the average of measurements acquired within the central portion of the rock sample ($L = 20 - 60$ mm, 2379 voxels). Lines are polynomial fits and crosses represent extrapolated residual NWP saturation values ($S_{\text{nw,r}}$). All experimental data values are provided in Table 1.
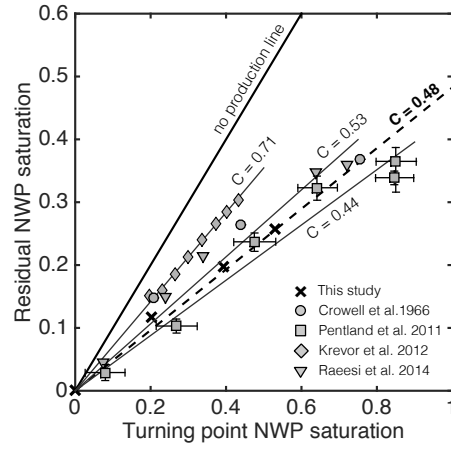
Figure 7: Initial-Residual (IR) plot showing residual NWP saturation as a function of the turning point NWP saturation for Berea Sandstone. Data from this study are for the $scCO_2$-water fluid pair and correspond to the average of measurements acquired within the central portion of the rock sample ($L = 20 - 60$ mm, 2379 voxels). These are compared to results reported in previous studies with various fluid pairs, namely $scCO_2$-brine (squares) (Pentland et al., 2011) and (diamonds) (Krevor et al., 2012), air-brine (triangles) (Raeesi et al., 2014) and air-water (circles) (Crowell et al., 1966). The corresponding linear model fits ($\widehat{S}_{\text{nw,r}} = C\widehat{S}_{\text{nw,turn}}$) are also shown (this study: $C = 0.48$ and $S_{\text{w,irr}} = 0.302$, dashed line).
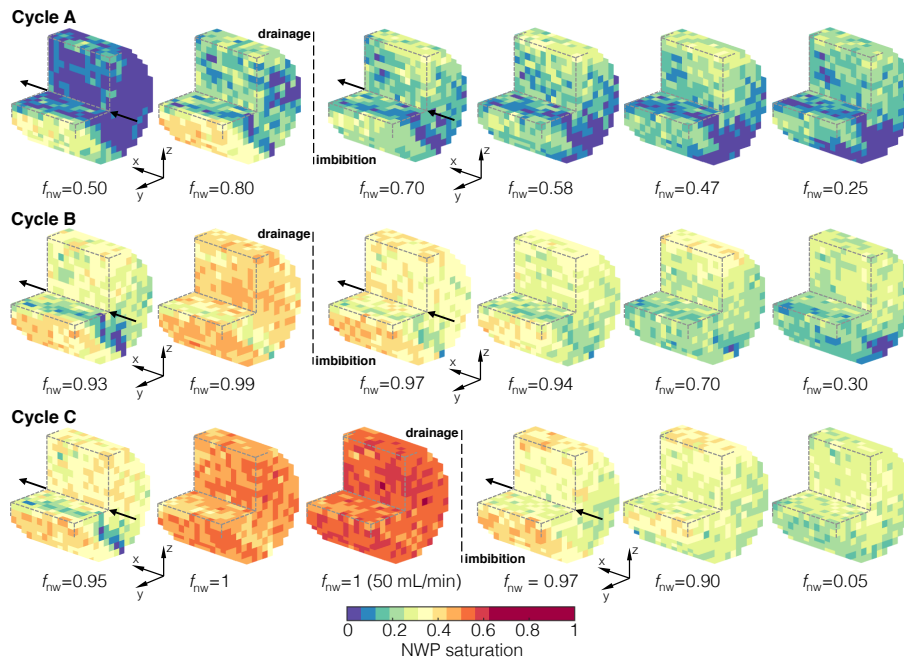
Figure 8: Steady-state 3D NWP saturation maps at various fractional flows (f_{nw}) for Cycles A, B and C, which all include both drainage and imbibition displacements. The maps represent the central portion of the core sample ($L = 20 - 60$ mm, 2379 voxels, see Figure 4). Voxel dimensions are $(3 \times 3 \times 3)$ mm^3 and at this resolution saturations are obtained with a precision of $S_{\mathrm{nw}} \pm 0.034$.
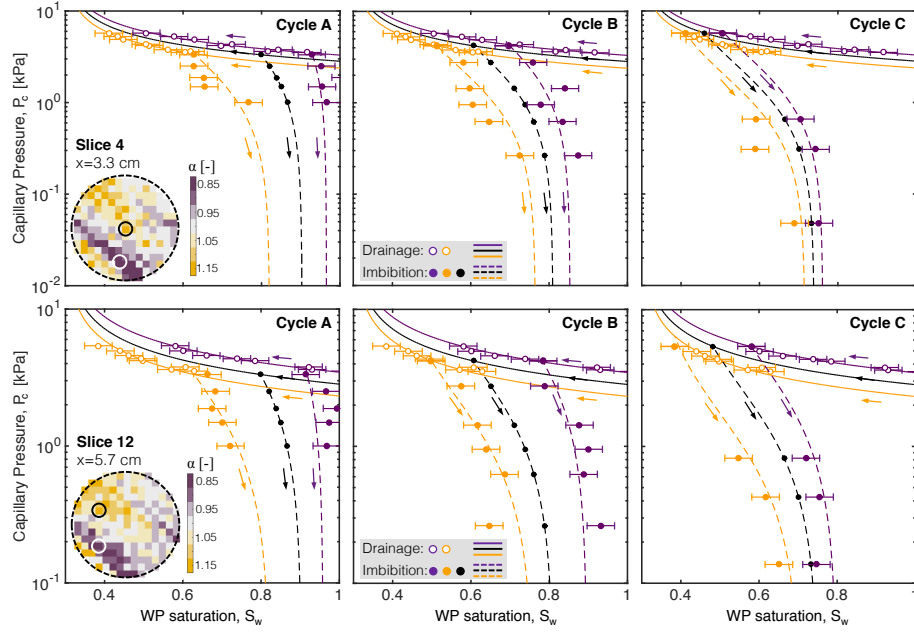
Figure 9: Voxel-by-voxel capillary pressure-saturation curves for four distinct voxels (dimensions: $(3\times3\times3)$ mm^3) undergoing the sequence of three drainage/imbibiton cycles and located within two separate slices, namely Slice 4 ($x = 3.3$ cm, upper row) and Slice 12 ($x = 5.7$ cm, bottom row). The horizontal error-bars indicate uncertainty of one standard deviation in the measured saturation ($S \pm \sigma_S$, with $\sigma_S = 0.034$). Core- (in black) and voxel-scale (in colour) Brooks-Corey $P_c - S_w$ curves are also shown for both drainage (fitted) and imbibition (predicted) branches. The 2D map shown in the inset represents the distribution of the P_c-scaling factor (α_i) for the given slice and provides the location for the selected voxels.
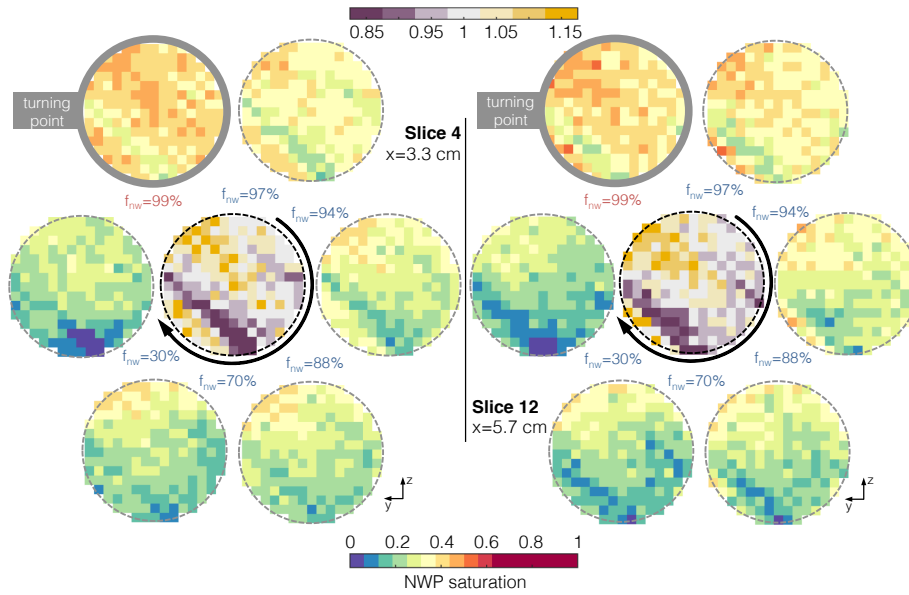
Figure 10: Steady-state 2D NWP saturation maps of two distinct slices (located at $x = 33$ mm and $x = 57$ mm) acquired during the full imbibition sequence of cycle B ($f_{\mathrm{nw}} = 0.99 - 0.3$). Voxel dimensions are $(3 \times 3 \times 3)$ mm^3 and at this resolution saturations are obtained with a precision of $S_{\mathrm{nw}} \pm 0.034$. The central 2D maps represent the distribution of the P_{c}-scaling factor (α_i) for the given slice.
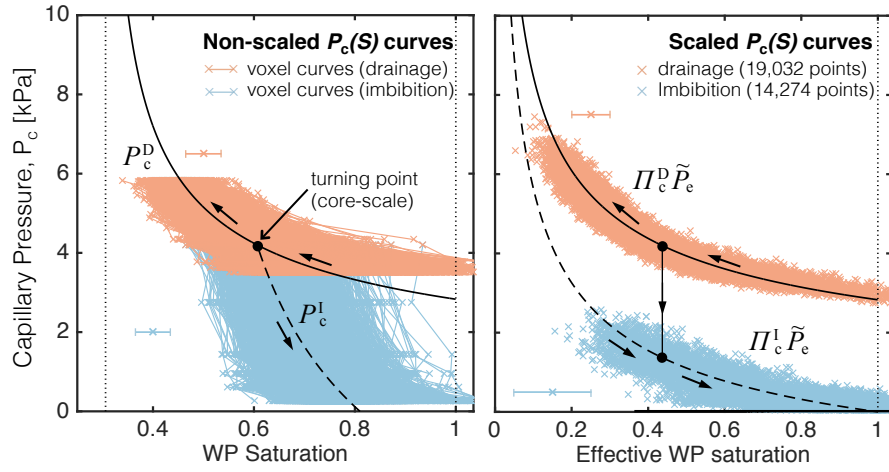
Figure 11: Non-scaled (left) versus scaled (right) capillary pressure curves for all voxels located within the central portion of the rock sample ($L = 20 - 60$ mm, 2379 voxels, each of them having dimensions $(3 \times 3 \times 3)$ mm^3). Drainage data (in red) include all three cycles (A, B and C), while imbibition data (in blue) are shown for cycle B only. The solid (drainage) and dashed (imbibition) black lines represent the mean (core-scale) curve against which observations at the voxel scale (coloured crosses) are scaled. Effective ($\widehat{S}_{\mathrm{w}}$) and effective *mobile* saturation values ($\widehat{S}_{\mathrm{nw,m}}$) are obtained with a precision of 0.049 and 0.10, respectively, as given by the illustrative horizontal error bars shown in each figure.
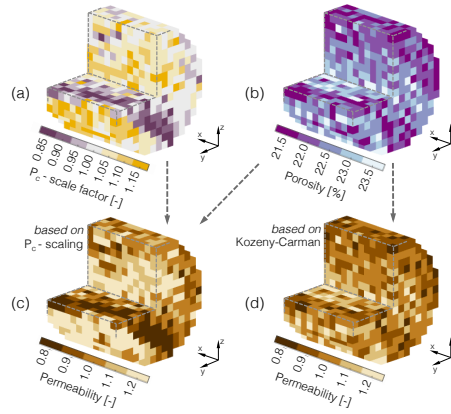
Figure 12: 3D representation of the central portion of the rock sample ($L = 20 - 60$ mm, 2379 voxels) in terms of (a) P_{c}-scaling factor, α, (b) porosity, ϕ_i, and (c)-(d) (normalised) permeability, k_i/k_0 (with k_0 being the measured core-scale permeability). Sub-core scale permeability values been computed using the J-Leverett (d) and Kozeny-Carman (c) scaling laws (see Section 6). For the latter $k_i = S_{\mathrm{K}} \phi_i^3 / \left(1 - \phi_i^2\right)$, where S_{K} is a constant parameter found using core-averaged data ($S_{\mathrm{K}} = 5.4 \times 10^4$ mD in this study). Voxel dimensions: ($3 \times 3 \times 3$) mm^3.
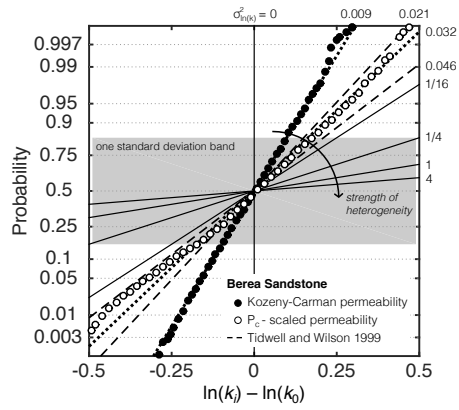
Figure 13: Normal probability plot for the voxel-permeability data sets shown in Figure 12 and derived from the Kozeny-Carman (filled circles, $\sigma^2_{\ln k} = 0.009$) and the J-Leverett scaling laws (empty circles, $\sigma^2_{\ln k} = 0.032$)). Permeability values are plotted as $\ln(k_i/k_0)$ and the dotted lines show the behaviour expected for a variable that follows a normal distribution with variance $\sigma^2_{\ln k}$. The dashed lines represent two sets of experimental results ($\sigma^2_{\ln k} = 0.021 - 0.046$) obtained on Berea Sandstone using a mini-permeameter (Tidwell and Wilson, 1999). The solid lines are illustrative examples of permeability distributions with stronger heterogeneity contrasts, namely $\sigma^2_{\ln k} = 1/16, 1/4, 1, 4$.